
ROBUST ELASTIC FULL WAVEFORM INVERSION USING ALTERNATING DIRECTION METHOD OF MULTIPLIERS WITH RECONSTRUCTED WAVEFIELDS

Kamal Aghazade

Formerly at the Institute of Geophysics, University of Tehran, Tehran, Iran
Currently at the Institute of Geophysics, Polish Academy of Sciences, Warsaw, Poland.
aghazade.kamal@igf.edu.pl

Ali Gholami

Institute of Geophysics, Polish Academy of Sciences, Warsaw, Poland,
agholami@igf.edu.pl (corresponding author)

Hossein S. Aghamiry

Charité Universitätsmedizin Berlin
Center for Biomedicine, Berlin, Germany. hossein.aghamiry@charite.de

Hamid Reza Siahkoohi

Institute of Geophysics, University of Tehran, Tehran, Iran.
hamid@ut.ac.ir

April 12, 2024

ABSTRACT

Elastic full-waveform inversion (EFWI) is a process used to estimate subsurface properties by fitting seismic data while satisfying wave propagation physics. The problem is formulated as a least-squares data fitting minimization problem with two sets of constraints: Partial-differential equation (PDE) constraints governing elastic wave propagation and physical model constraints implementing prior information. The alternating direction method of multipliers is used to solve the problem, resulting in an iterative algorithm with well-conditioned subproblems. Although wavefield reconstruction is the most challenging part of the iteration, sparse linear algebra techniques can be used for moderate-sized problems and frequency domain formulations. The Hessian matrix is blocky with diagonal blocks, making model updates fast. Gradient ascent is used to update Lagrange multipliers by summing PDE violations. Various numerical examples are used to investigate algorithmic components, including model parameterizations, physical model constraints, the role of the Hessian matrix in suppressing interparameter cross-talk, computational efficiency with the source sketching method, and the effect of noise and near-surface effects.

1 Introduction

Full waveform inversion (FWI) is a widely used seismic imaging technique for estimating the elastic properties of the subsurface by inverting seismic data recorded at or near the surface. The modeling process is based on solving the wave equation (Tarantola, 1984). The inverse process involves a non-linear optimization problem, and due to the computational cost, it typically uses a local optimization strategy to iteratively modify the properties of the medium (for a comprehensive review, see Virieux and Operto, 2009). The fidelity of the resulting property estimates hinges upon

the interplay between accurate forward modeling, which meticulously incorporates the physics of wave propagation, and the efficacy of the chosen inverse optimization method.

Initially, FWI applications considered either the acoustic approximation (Tarantola, 1984; Gauthier et al., 1986) or the elastic isotropic approximation (Mora, 1988) of the Earth’s interior. Acoustic FWI assuming a constant density was preferred for field records since the unconverted P-wave velocity (V_P) could describe most features in the data (e.g., Ravaut et al., 2004; Operto et al., 2006). However, traditional acoustic FWI methods overlook the presence of S-waves in the data (Prioux et al., 2011). This limitation leads to inaccurate modeling of physics and introduces residual data artifacts (Mulder and Plessix, 2008). Previous studies have attempted to address these issues by considering density as a proxy variable in acoustic FWI, which partially accounts for dynamic elastic effects and helps mitigate overfitting of elastic data caused by incorrect V_P variations (Borisov et al., 2014). Despite these efforts, acoustic inversion still faces challenges in accurately modeling amplitude variation with offset effects, particularly for wide aperture data (Barnes and Charara, 2008, 2009). This is due to amplitude errors arising from the differences between the recorded particle velocities and pressure fields, as well as the directivity of the sources and receivers. Addressing these limitations and achieving a more accurate subsurface characterization require the development of robust and efficient inversion techniques that account for the complete elastic forward modeling. Recent advances in computational power and the acquisition of multicomponent data have enabled multiparameter inversion, where different classes of parameters can be incorporated into the FWI procedure (Sears et al., 2008; Prioux et al., 2013a,b; Operto et al., 2013; Vigh et al., 2014).

Despite increasing the accuracy of physics of wave propagation, transitioning from acoustic to elastic inversion poses challenges that must be addressed appropriately. The sensitivity of the inversion for one parameter class may differ significantly from another, and adding more parameters introduces more degrees of freedom, potentially increasing the degree of ill-posedness. Cross-talk, which refers to the coupling between different parameter classes as a function of the scattering angle, is another issue in multiparameter inversion. Parameters with different natures may have similar signatures on the data, and this can be quantified using tools such as radiation pattern analysis (Forgues and Lambaré, 1997; Kazei and Alkhalifah, 2019) or sensitivity kernel analysis (Pan et al., 2019). Several strategies have been proposed to address parameter cross-talk, including model/data-driven approaches, model reparameterization, the use of the inverse of the Hessian matrix, and decomposition of the P- and S-wave modes (Gholami et al., 2013; Métivier et al., 2014; Wang and Cheng, 2017; Wang et al., 2018, 2019).

Once the forward modeling operator is established, the parameter estimation task transforms into a nonlinearly constrained optimization problem (Haber et al., 2000). This optimization objective aims to minimize the data misfit while adhering to nonlinear constraints dictated by the wave equation. Various techniques, including Lagrangian, penalty, and Augmented Lagrangian (AL) methods, can be employed to address such constrained problems (Nocedal and Wright, 2006). Additionally, optimization can be approached through either reduced space or full space methods. In the former, optimization exclusively involves model parameters, while the latter includes wavefields and Lagrange multipliers. Owing to superior memory efficiency, the majority of FWI algorithms opt for the reduced space approach (Bunks et al., 1995; Operto et al., 2006; Brossier et al., 2009; Köhn et al., 2012; Duan and Sava, 2016).

However, reduced space FWI encounters cycle skipping (local minima), a challenge exacerbated in Elastic FWI (EFWI) by the propagation of short-wavelength S-waves. To address this issue, early studies primarily relied on low-frequency data (below 3 Hz) (e.g., Choi et al., 2008; Brossier et al., 2009; Köhn et al., 2012) or implemented model-driven workflows. These workflows, such as using hydrophone data to recover long-to-intermediate wavelengths of S-wave velocity (V_S), were instrumental in establishing optimal initial models for subsequent inversion phases (see e.g., Prioux et al., 2013b). Inversion processes often adopt a multiscale approach, commencing with low frequencies and gradually progressing to higher frequencies, to mitigate the impact of cycle skipping (Bunks et al., 1995).

When confronting seismic data lacking low-frequency components, EFWI may utilize the low-frequency component of the damped wavefield in the Laplace-Fourier domain (Jun et al., 2014). Nevertheless, the presence of undesirable cross-correlation components can distort the gradient, particularly in scenarios like low-velocity zones beneath salt, potentially yielding low-resolution and inaccurate models (Kwon et al., 2017). Machine-learning (ML) tools have been explored to extrapolate low-frequency data (Sun and Demanet, 2021); however, their utilization often involves significant computational costs and remains an active area of research. Phase tracking, as used by Li and Demanet (2015), enhances inversion robustness in the absence of low frequencies, particularly in dispersion-free media. To address cycle skipping, researchers, such as Chi et al. (2014) and Zhang and Li (2022), have turned to envelope-based inversion through wave mode decomposition. However, envelope inversion grapples with instabilities in both the gradient term and the adjoint source (Xiong et al., 2023). Combining envelope inversion with deconvolution, as proposed by Chen et al. (2022), considers phase shifts and mitigates artificial side lobes in data due to the loss of low-frequency components. Phase correction methods, employed by researchers like Chi et al. (2014) and Hu et al. (2022), address

phase differences between modeled and synthetic data. Another strategy involves modifying the misfit function; for instance, [Zhang and Alkhalifah \(2019\)](#) introduced a local cross-correlation objective function to overcome the susceptibility to cross-talk from neighboring arrivals. The application of optimal transport misfit functions, proposed in some studies ([Marty et al., 2022](#); [Borisov et al., 2022](#)), faces challenges, especially when comparing signed and oscillatory signals in elastic media.

The challenge of local minima in reduced space FWI can also be effectively addressed using penalty or AL formulations in the full space. For acoustic FWI, [van Leeuwen and Herrmann \(2013\)](#) applied the penalty formulation, leading to the Wavefield Reconstruction Inversion (WRI) algorithm, whereas [Aghamiry et al. \(2019, 2020\)](#) utilized the AL formulation, resulting in the iteratively refined WRI (IR-WRI) algorithm. Extensive numerical results have demonstrated a substantial enhancement in stability and convergence with these algorithms compared to traditional reduced-space FWI (see [Operto et al., 2023](#), and references therein). Moreover, algorithms based on AL methods outperform penalty methods in terms of stability and convergence (for a detailed comparison between them, see [Gholami, 2023](#),).

The AL (AL) formulation provides a comprehensive framework for addressing challenges in EFWI, encompassing issues of ill-posedness, cross-talk, and convergence. Leveraging the Alternating Direction Method of Multipliers (ADMM) ([Gabay and Mercier, 1976](#); [Boyd et al., 2011](#)), the resulting algorithm facilitates the integration of the Hessian matrix to mitigate cross-talk, incorporates regularization techniques to alleviate ill-posedness ([Lin and Huang, 2014](#)), and demonstrates robust convergence even from inaccurate initial models, all while maintaining computational efficiency. To adapt the ADMM method to elastic media, we explore various parameterizations, including Lamé parameters and velocities, with density set as a constant. As demonstrated later, in both cases, the associated Gauss-Newton Hessian matrix exhibits a block-diagonal sparse structure that allows explicit inversion, enabling an exploration of its role in reducing interparameter cross-talk. Additionally, we introduce a source sketching method, previously developed for acoustic FWI, to enhance the computational efficiency of the algorithm.

Furthermore, we incorporate physical constraints into the EFWI inversion process to promote physically plausible models ([Duan and Sava, 2016](#)). One such methodology involves the use of seismic facies information built by clustering seismic characteristics and spatial coherence within the framework of FWI ([Zhang et al., 2018](#)). Another approach involves using the relationships between the parameters in the elastic medium based on borehole data or empirical equations derived from laboratory measurements ([Brocher, 2005](#)). We optimize the model parameters so that they are at the intersection of these constraints, and this problem is efficiently addressed using the ADMM method. We present numerical examples using benchmark models to demonstrate the performance of the proposed EFWI algorithm.

2 Preliminaries

The basic definitions and symbols used in this paper are as follows. The field of real and complex numbers are denoted by \mathbb{R} and \mathbb{C} , respectively. Vectors and matrices are represented by bold lowercase and uppercase letters, respectively. The number of discrete model parameters (for each class), the number of receivers, and the number of sources are denoted by n , n_r , and n_s , respectively. The angular frequency is denoted by $\omega = 2\pi f$, where f is the frequency. The identity and diagonal matrices are denoted by \mathbf{I} and $\text{diag}(\bullet)$, respectively. The second-order partial derivative with respect to variable i is represented by ∂_{ii} , and the mixed derivative with respect to variables i and j is represented by ∂_{ij} . The conjugate transpose of a matrix/vector is denoted by the superscript T . The symbol \circ denotes the Hadamard (element-wise) multiplication. In this paper, $(\bullet)^k$ represents the value of (\bullet) at iteration k .

3 Theory

We consider the following frequency-domain isotropic elastic wave equation:

$$\rho\omega^2\mathbf{u}_x + (\lambda + 2\mu)\partial_{xx}\mathbf{u}_x + \mu\partial_{zz}\mathbf{u}_x + (\lambda + \mu)\partial_{xz}\mathbf{u}_z = \mathbf{b}_x, \quad (1a)$$

$$\rho\omega^2\mathbf{u}_z + (\lambda + 2\mu)\partial_{zz}\mathbf{u}_z + \mu\partial_{xx}\mathbf{u}_z + (\lambda + \mu)\partial_{xz}\mathbf{u}_x = \mathbf{b}_z, \quad (1b)$$

where $\rho \in \mathbb{R}^{n \times 1}$ is mass density, $\lambda \in \mathbb{R}^{n \times 1}$ and $\mu \in \mathbb{R}^{n \times 1}$ denote Lamé parameters, $\mathbf{u}_x \in \mathbb{C}^{n \times 1}$ and $\mathbf{u}_z \in \mathbb{C}^{n \times 1}$ are horizontal and vertical particle displacements, and $\mathbf{b}_x \in \mathbb{C}^{n \times 1}$, $\mathbf{b}_z \in \mathbb{C}^{n \times 1}$ are the source terms. Equation 1 can be written in compact algebraic form as:

$$\mathbf{A}(\mathbf{m})\mathbf{u} = \mathbf{b}, \quad (2)$$

where

$$\mathbf{m} = \begin{pmatrix} \lambda \\ \mu \\ \rho \end{pmatrix}, \quad \mathbf{u} = \begin{pmatrix} \mathbf{u}_x \\ \mathbf{u}_z \end{pmatrix}, \quad \mathbf{b} = \begin{pmatrix} \mathbf{b}_x \\ \mathbf{b}_z \end{pmatrix}, \quad (3)$$

and

$$\mathbf{A}(\mathbf{m}) = \begin{pmatrix} \omega^2 \text{diag}(\boldsymbol{\rho}) + \text{diag}(\boldsymbol{\varpi})\partial_{xx} + \text{diag}(\boldsymbol{\mu})\partial_{zz} & \text{diag}(\boldsymbol{\lambda} + \boldsymbol{\mu})\partial_{xz} \\ \text{diag}(\boldsymbol{\lambda} + \boldsymbol{\mu})\partial_{xz} & \omega^2 \text{diag}(\boldsymbol{\rho}) + \text{diag}(\boldsymbol{\varpi})\partial_{zz} + \text{diag}(\boldsymbol{\mu})\partial_{xx} \end{pmatrix}, \quad (4)$$

denotes the complex-valued impedance matrix, where $\boldsymbol{\varpi} = \boldsymbol{\lambda} + 2\boldsymbol{\mu}$.

In order to estimate the subsurface model parameters \mathbf{m} , we formulate the elastic FWI as the following constrained optimization problem:

$$\begin{aligned} & \underset{\mathbf{m}, \mathbf{u}}{\text{minimize}} && \frac{1}{2} \|\mathbf{P}\mathbf{u} - \mathbf{d}\|_2^2 \\ & \text{subject to} && \mathbf{A}(\mathbf{m})\mathbf{u} = \mathbf{b}, \\ & && \mathbf{m} \in C_1 \cap C_2 \end{aligned} \quad (5)$$

where

$$\mathbf{P} = \begin{pmatrix} \tilde{\mathbf{P}} & \mathbf{0} \\ \mathbf{0} & \tilde{\mathbf{P}} \end{pmatrix}, \quad \mathbf{d} = \begin{pmatrix} \mathbf{d}_x \\ \mathbf{d}_z \end{pmatrix}, \quad (6)$$

and the observation operator $\tilde{\mathbf{P}}$ samples the wavefield at receiver locations. C_1 and C_2 are two convex sets built from prior physical information about the model parameters. Specifically, C_1 defines a box in the plane formed by $(\mathbf{m}_p, \mathbf{m}_s)$ with lower bound $(\underline{\mathbf{m}}_p, \underline{\mathbf{m}}_s)$ and upper bound $(\overline{\mathbf{m}}_p, \overline{\mathbf{m}}_s)$. Also, C_2 is defined as the set of points between two lines $\underline{a}\mathbf{m}_p + \underline{b}\mathbf{m}_s = \underline{c}$ and $\overline{a}\mathbf{m}_p + \overline{b}\mathbf{m}_s = \overline{c}$, where the parameters $(\underline{a}, \underline{b}, \underline{c})$ and $(\overline{a}, \overline{b}, \overline{c})$ can be found according to the borehole information or empirical relations (Brocher, 2005; Duan and Sava, 2016). The intersection of C_1 and C_2 forms a convex set as shown in Figure 1.

Satisfying such constraints can be achieved by solving the corresponding convex feasibility problem by projecting the updated models onto the intersection of nonempty, closed, and convex sets. One simple approach to solve the feasibility problem is von Neumann's alternating projection method (also known as the projection onto convex sets, POCS), which was used by Baumstein (2013) for the case of anisotropic acoustic inversion. Another variant of alternating projection with slight differences by introducing auxiliary variables is Dykstra's algorithm (Dykstra, 1983).

From equation 5 one can derive the AL (Powell, 1969)

$$\mathcal{L}_\beta(\mathbf{u}, \mathbf{m}, \boldsymbol{\eta}) = \frac{1}{2} \|\mathbf{P}\mathbf{u} - \mathbf{d}\|_2^2 - \boldsymbol{\eta}^T [\mathbf{A}(\mathbf{m})\mathbf{u} - \mathbf{b}] + \frac{\beta}{2} \|\mathbf{A}(\mathbf{m})\mathbf{u} - \mathbf{b}\|_2^2. \quad (7)$$

In this equation, $\mathcal{L}_\beta(\mathbf{u}, \mathbf{m}, \boldsymbol{\eta})$ consists of three terms. The first term is the data misfit term, quantifying the discrepancy between the modeled data $\mathbf{P}\mathbf{u}$ and the observed data \mathbf{d} . The second term, a Lagrangian term, introduces the Lagrange multiplier vector $\boldsymbol{\eta}$ to enforce satisfaction of the wave equation constraint. To enhance optimization stability, the third term, a penalty term, is added, controlled by the penalty parameter $\beta > 0$. The adjustment of β penalizes the Lagrange multipliers, contributing to optimization stability (Gholami, 2023).

Notably, the choice of the negative sign in the Lagrangian term aligns with the convention set by Powell (1969). Although the optimization of the Lagrangian function alone might be prone to instability, the introduction of the penalty term through the AL technique significantly improves convergence. Importantly, this technique surpasses the penalty method, as the estimates of Lagrange multipliers in the AL approach tend to be more accurate. It is crucial to highlight that setting the Lagrange multiplier term to zero reverts to the penalty formulation used in the WRI approach (van Leeuwen and Herrmann, 2013). The optimization of the AL function is effectively addressed through dual ascent methods within the framework of the wavefield-oriented ADMM (Boyd et al., 2011; Gholami, 2023):

$$\mathbf{u}^{k+1} = \arg \min_{\mathbf{u}} \mathcal{L}_\beta(\mathbf{u}, \mathbf{m}^k, \mathbf{s}^k), \quad (8a)$$

$$\mathbf{m}^{k+1} = \arg \min_{\mathbf{m} \in C_1 \cap C_2} \mathcal{L}_\beta(\mathbf{u}^{k+1}, \mathbf{m}, \mathbf{s}^k), \quad (8b)$$

$$\mathbf{s}^{k+1} = \mathbf{s}^k + \mathbf{b} - \mathbf{A}(\mathbf{m}^{k+1})\mathbf{u}^{k+1}, \quad (8c)$$

where $\mathbf{s}^k = \frac{1}{\beta} \boldsymbol{\eta}^k$ is the scaled dual variable. In the following subsections, we provide the detailed analysis for solving these subproblems.

3.1 Wavefield reconstruction step

The optimization problem in 8a is quadratic in \mathbf{u} , and its minimization leads to the following linear system of equations:

$$\left[\beta \mathbf{A}^T(\mathbf{m}^k) \mathbf{A}(\mathbf{m}^k) + \mathbf{P}^T \mathbf{P} \right] \mathbf{u}^{k+1} = \beta \mathbf{A}^T(\mathbf{m}^k) (\mathbf{b} + \mathbf{s}^k) + \mathbf{P}^T \mathbf{d}. \quad (9)$$

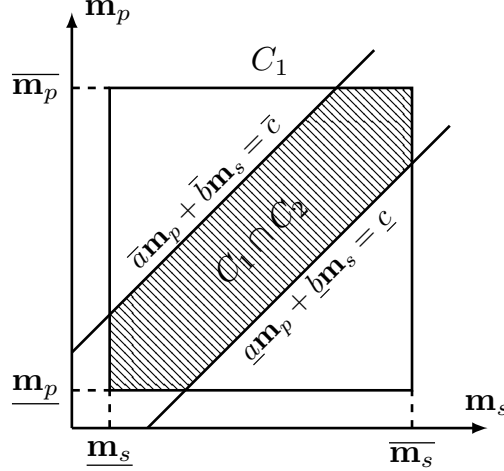


Figure 1: The sets C_1 and C_2 and the related parameters. The filled area shows the desired set.

where the size of this system is twice the size of the system that appears in acoustic inversion (van Leeuwen and Herrmann, 2013; Aghamiry et al., 2019). If the problem size is small to moderate, this system can be solved explicitly using LU factorization. However, for larger problems, iterative methods with appropriate preconditioners should be used to solve this data-assimilated wave equation. For 3D applications, the time-domain implementation is recommended. However, tackling equation 9 in the time-domain poses a substantial challenge due to the absence of explicit time-stepping and the escalating computational and memory demands associated with larger models. This challenge arises from the inherently high-dimensional nature of the wavefield. A more efficient alternative approach involves adopting an equivalent multiplier-oriented formulation. In this strategy, we first solve a normal system of data size to obtain least-square multipliers. Subsequently, the wavefields are computed straightforwardly using time-stepping (see Gholami et al., 2022; Gholami, 2023).

3.2 Model estimation step

Different parameterizations can be used to update model parameters in elastic waveform inversion (Tarantola, 1986). The Lamé parameters (λ , μ) and density (ρ) are commonly used for defining an elastic isotropic medium. However, density reconstruction poses challenges due to parameter trade-off, poor sensitivity of waveform mismatch to the density perturbation, and difficulties in retrieving the low-wavenumber component of density (Köhn et al., 2012; Sun et al., 2017; Pan et al., 2018). In this study, we consider a constant density medium and explore parameterizations based on (λ , μ) and (\mathbf{V}_P^2 , \mathbf{V}_S^2) for model update, where for the $\mathbf{m} = (\mathbf{V}_P^2, \mathbf{V}_S^2)$ parameterization, the relations $\lambda = \rho \mathbf{V}_P^2 - 2\mathbf{V}_S^2$ and $\mu = \rho \mathbf{V}_S^2$ are used. Regarding the model estimation problem, we can write:

$$\mathbf{A}(\mathbf{m})\mathbf{u}^{k+1} - \mathbf{b} - \mathbf{s}^k = \underbrace{\begin{bmatrix} \mathbf{L}_{11} & \mathbf{L}_{12} \\ \mathbf{L}_{21} & \mathbf{L}_{22} \end{bmatrix}}_{\mathbf{L}(\mathbf{u}^{k+1})} \underbrace{\begin{bmatrix} \mathbf{m}_1 \\ \mathbf{m}_2 \end{bmatrix}}_{\mathbf{m}} - \underbrace{\begin{bmatrix} \mathbf{y}_x \\ \mathbf{y}_z \end{bmatrix}}_{\mathbf{y}(\mathbf{u}^{k+1})}, \quad (10)$$

Then, for each mentioned parameterization, the updated parameters are obtained by solving the following least squares problem:

$$\mathbf{m}^{k+1} = \arg \min_{\mathbf{m}} \|\mathbf{L}\mathbf{m} - \mathbf{y}\|_2^2, \quad (11)$$

where $\mathbf{L} \equiv \mathbf{L}(\mathbf{u}^{k+1})$ and $\mathbf{y} \equiv \mathbf{y}(\mathbf{u}^{k+1})$. This least-squares problem admits the closed-form solution:

$$\mathbf{m}^{k+1} = [\mathbf{L}^T \mathbf{L}]^{-1} \mathbf{L}^T \mathbf{y}. \quad (12)$$

The structure of the operator \mathbf{L} and vector \mathbf{y} are presented in Table 1 for different parameterizations. The operator \mathbf{L} is a 2 by 2 block matrix with diagonal blocks. Consequently, the sparsity pattern and straightforward calculation process facilitate the explicit computation of the inverse of the Gauss-Newton Hessian matrix $\mathbf{L}^T \mathbf{L}$ (Figure 2).

We also consider the parameterization (\mathbf{V}_P , \mathbf{V}_S). Mathematical formulas for the model update in this case are presented in Appendix A. In Appendix B, we provide the detailed formulation for solving the model subproblem by including physical constraints.

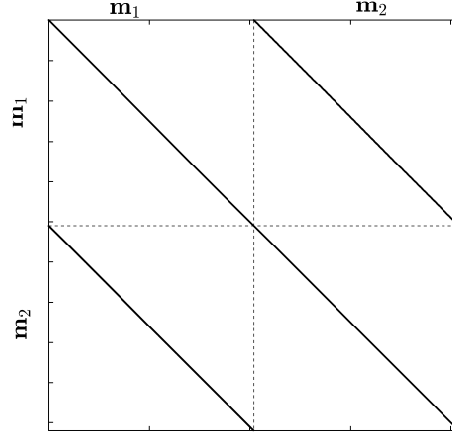


Figure 2: Hessian structure for two-parameters problem. The main-diagonal blocks and off-diagonal blocks of $\beta \mathbf{L}^T \mathbf{L}$ respectively include $\frac{\partial^2 \mathcal{L}}{\partial \mathbf{m}_i \partial \mathbf{m}_i}$ and $\frac{\partial^2 \mathcal{L}}{\partial \mathbf{m}_i \partial \mathbf{m}_j}$, in which i, j denote the index of each parameter class.

Table 1: The structure of matrix \mathbf{L} and vector \mathbf{y} for $(\boldsymbol{\lambda}, \boldsymbol{\mu})$ and $(\mathbf{V}_P^2, \mathbf{V}_S^2)$ parameterization.

	$\mathbf{L}(\mathbf{u}) \in \mathbb{C}^{2n \times 2n}$		$\mathbf{y}(\mathbf{u}) \in \mathbb{C}^{2n \times 1}$	
$(\boldsymbol{\lambda}, \boldsymbol{\mu})$	$\text{diag}(\partial_{xx} \mathbf{u}_x) + \text{diag}(\partial_{xz} \mathbf{u}_z)$ $\text{diag}(\partial_{zz} \mathbf{u}_z) + \text{diag}(\partial_{xz} \mathbf{u}_x)$	$\text{diag}(2\partial_{xx} \mathbf{u}_x) + \text{diag}(\partial_{zz} \mathbf{u}_x) + \text{diag}(\partial_{xz} \mathbf{u}_z)$ $\text{diag}(2\partial_{zz} \mathbf{u}_z) + \text{diag}(\partial_{xx} \mathbf{u}_z) + \text{diag}(\partial_{xz} \mathbf{u}_x)$	$\mathbf{b}_x + \mathbf{s}_x^k$ $\mathbf{b}_z + \mathbf{s}_z^k$	$-\omega^2 \boldsymbol{\rho} \mathbf{u}_x$ $-\omega^2 \boldsymbol{\rho} \mathbf{u}_z$
$(\mathbf{V}_P^2, \mathbf{V}_S^2)$	$\text{diag}(\partial_{xx} \mathbf{u}_x \circ \boldsymbol{\rho}) + \text{diag}(\partial_{xz} \mathbf{u}_z \circ \boldsymbol{\rho})$ $\text{diag}(\partial_{zz} \mathbf{u}_z \circ \boldsymbol{\rho}) + \text{diag}(\partial_{xz} \mathbf{u}_x \circ \boldsymbol{\rho})$	$\text{diag}(\partial_{zz} \mathbf{u}_x \circ \boldsymbol{\rho}) - \text{diag}(\partial_{xz} \mathbf{u}_z \circ \boldsymbol{\rho})$ $\text{diag}(\partial_{xx} \mathbf{u}_z \circ \boldsymbol{\rho}) - \text{diag}(\partial_{xz} \mathbf{u}_x \circ \boldsymbol{\rho})$	$\mathbf{b}_x + \mathbf{s}_x^k$ $\mathbf{b}_z + \mathbf{s}_z^k$	$-\omega^2 \boldsymbol{\rho} \mathbf{u}_x$ $-\omega^2 \boldsymbol{\rho} \mathbf{u}_z$

3.3 Dual ascent step

To mitigate the instability issue during early iterations, a damped multiplier update can be employed, as suggested by [Gholami et al. \(2023\)](#). This update can be applied by replacing the multiplier update in equation 8c with the following damped update:

$$\mathbf{s}^{k+1} = \left(\frac{k}{k + \xi} \right) (\mathbf{s}^k + \mathbf{b} - \mathbf{A}(\mathbf{m}^{k+1}) \mathbf{u}^{k+1}), \quad (13)$$

where ξ is a damping factor, typically chosen to be larger than 1. The damping factor can be adjusted based on the stability of the algorithm and the convergence behavior observed during the iterations. A larger damping factor can help stabilize the algorithm, but it may slow down convergence. On the other hand, a smaller damping factor may speed up convergence, but it can also introduce instability. By using the damped multiplier update, the ADMM algorithm can handle rough initial models more effectively and reduce the need for successive restarts, leading to improved convergence behavior ([Gholami et al., 2023](#)).

4 Numerical Example

In this section, the performance of the proposed algorithm is assessed through a set of numerical examples. The quality of the inversion results is quantified using several metrics, including the "source residual", "data residual", and "model error".

The "source residual" measures the discrepancy between the modeled sources computed using the updated model \mathbf{m}^{k+1} and the desired sources \mathbf{b} . It is computed as the Euclidean norm of the difference between the modeled sources and the desired sources. The "data residual", on the other hand, measures the mismatch between the observed data \mathbf{d} and the modeled data $\mathbf{P} \mathbf{u}^{k+1}$. It is computed as the Euclidean norm of the difference between the observed data and the modeled data. Finally, the "model error" quantifies the deviation between the estimated model \mathbf{m}^{k+1} and the true model \mathbf{m}^* . It is computed as the Euclidean norm of the difference between the estimated model and the true model.

These metrics provide quantitative measures of the accuracy of the inversion results. A smaller source residual and data residual indicate a better fit between the modeled and desired sources and data, respectively. Similarly, a smaller model

error indicates a closer resemblance between the estimated model and the true model. By evaluating these metrics, we can assess the effectiveness and reliability of the proposed algorithm in capturing the subsurface properties and recovering the true model. Moreover, the PDE operator, \mathbf{A} , is discretized using the optimal 9-point finite difference stencil proposed by [Chen and Cao \(2016\)](#).

4.1 Double circular toy model

4.1.1 On the role of parameterization

In the assessment of the model parameterization for constant density elastic media, double circular heterogeneities are considered for both the $(\mathbf{V}_P, \mathbf{V}_S)$ and (λ, μ) parameterizations. These heterogeneities are located at different positions and embedded in a homogeneous background model, as shown in Figure 3a and Figure 3b, respectively. It is important to note that for this analysis, velocity models were not constructed using Lamé parameters. The primary goal here is to investigate the potential cross-talk between the different parameterizations and assess their impact. The circular acquisition setup (with radius of 1 km) consists of 16 vertically directed forces, denoted as \mathbf{b}_z , which emit a Ricker wavelet with a dominant frequency of 10 Hz. The wavefields are recorded by 128 two-component receivers. To prevent any reflection artifacts, absorbing boundary conditions are implemented along the four sides of the modeling domain.

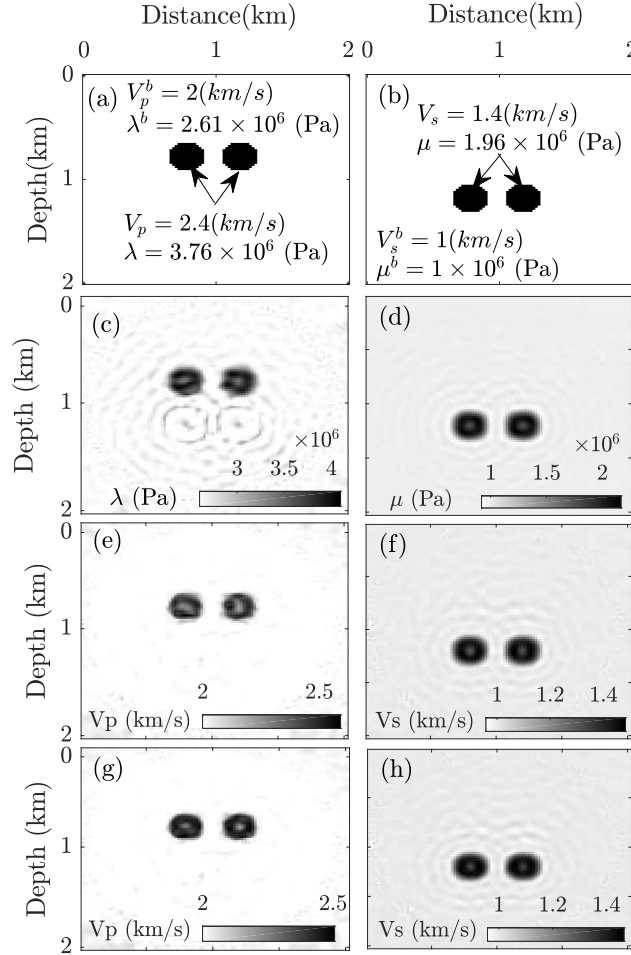


Figure 3: Double circular model. (a-b) True $(\mathbf{V}_P, \mathbf{V}_S)$ and (λ, μ) models, in which parameters with superscripts (b) indicate the background values. The estimated models obtained with parameterization (λ, μ) (c-d), $(\mathbf{V}_P, \mathbf{V}_S)$ (e-f) and $(\mathbf{V}_P^2, \mathbf{V}_S^2)$ (g-h) after 70 iterations.

In the analysis, background models were used to perform inversion for two frequencies, specifically 2.5 Hz and 5 Hz, concurrently. Three different parameterizations were employed: (λ, μ) , $(\mathbf{V}_P, \mathbf{V}_S)$, and $(\mathbf{V}_P^2, \mathbf{V}_S^2)$. The results of the inversion after 70 iterations are shown in Figure 3c-d for the (λ, μ) parameterization, Figure 3e-f for the $(\mathbf{V}_P, \mathbf{V}_S)$

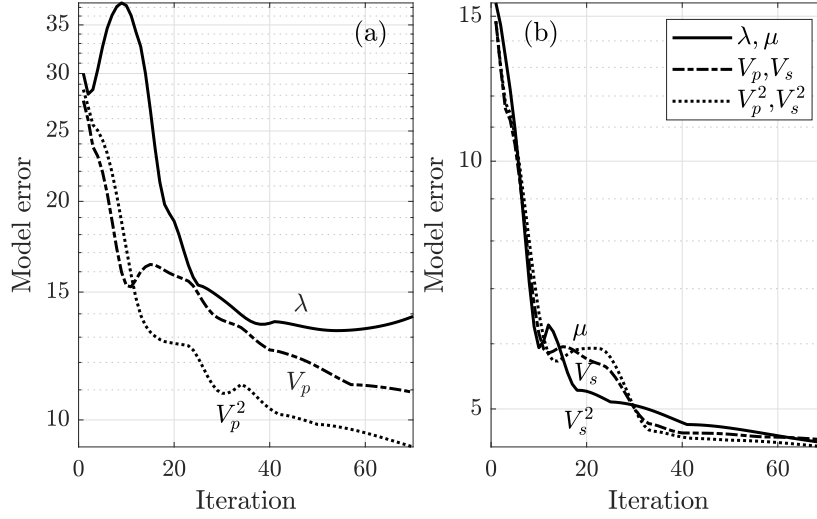


Figure 4: Double circular model. The evolution of the computed model errors during iteration for different model parameterizations: (a) $(\lambda, \mathbf{V}_P, \mathbf{V}_P^2)$, and (b) $(\mu, \mathbf{V}_S, \mathbf{V}_S^2)$.

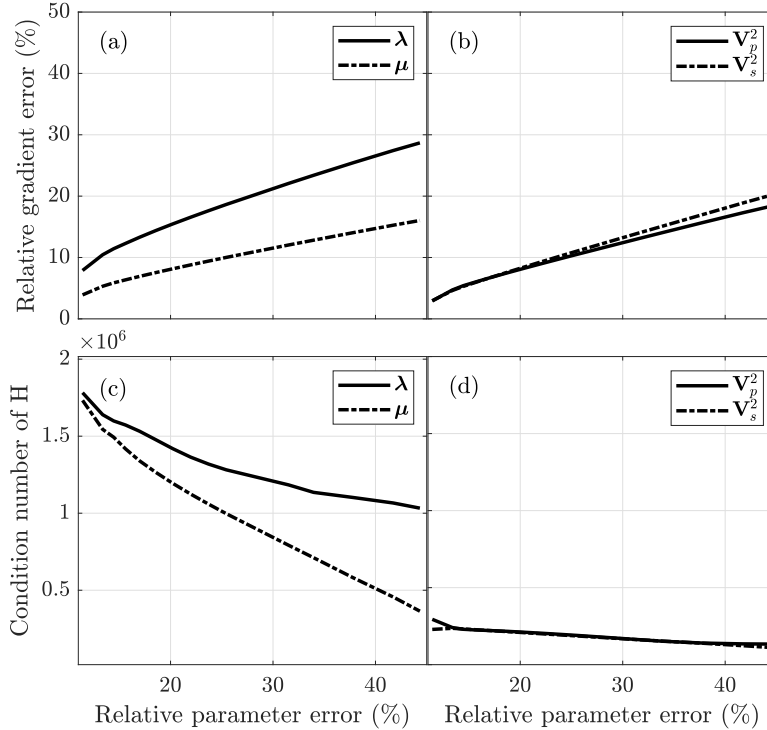


Figure 5: Sensitivity analysis for (λ, μ) and $(\mathbf{V}_P^2, \mathbf{V}_S^2)$ parameterizations. Relative error in the gradient vector versus the error in each parameter for (a) (λ, μ) and (b) $(\mathbf{V}_P^2, \mathbf{V}_S^2)$. The condition number of the Hessian matrix versus relative error of the input parameters for (c) (λ, μ) and (d) $(\mathbf{V}_P^2, \mathbf{V}_S^2)$.

parameterization, and Figure 3g-h for the $(\mathbf{V}_S^2, \mathbf{V}_S^2)$ parameterization. Generally, the inverted parameters obtained using $(\mathbf{V}_P, \mathbf{V}_S)$ and $(\mathbf{V}_P^2, \mathbf{V}_S^2)$ exhibit comparable accuracy. During the early iterations of the ADMM algorithm, all

parameterizations exhibit cross-talk, where the \mathbf{V}_S parameter influences \mathbf{V}_P and $\boldsymbol{\mu}$ influences $\boldsymbol{\lambda}$. However, as the iterations progress, these cross-talk effects are suppressed. There is a slight parameter leakage of $\boldsymbol{\mu}$ into $\boldsymbol{\lambda}$, but it can be regarded as noise and can be controlled through appropriate regularization techniques. Figure 4 illustrates the evolution of model errors versus iteration. It is worth noting that there is no significant parameter leakage observed in terms of velocity parameterization. This may be attributed to the influence of the Gauss-Newton Hessian matrix ($\mathbf{L}^T\mathbf{L}$), which will be discussed in the next section.

4.1.2 Sensitivity Analysis

In the analysis of model parameterization, the sensitivity of each parameter class is assessed to determine the more stable case between $(\boldsymbol{\lambda}, \boldsymbol{\mu})$ and $(\mathbf{V}_P^2, \mathbf{V}_S^2)$. The sensitivity analysis involves solving a linear system associated with each parameter class and perturbing one variable by a specific amount to analyze the resulting relative error in the gradient vector $\mathbf{L}^T\mathbf{y}$ and the condition number of the corresponding Hessian matrix $\mathbf{L}^T\mathbf{L}$. For this analysis, a surface acquisition geometry is considered. The \mathbf{V}_S model is constructed using a constant Poisson's ratio of 0.24, while the Lamé parameters are constructed in the same precise manner.

Figure 5 displays the calculated gradient error and condition number for a frequency of 3 Hz. The results show that the gradient vector is more sensitive to errors in $\boldsymbol{\lambda}$ in the case of the $(\boldsymbol{\lambda}, \boldsymbol{\mu})$ parameterization. In contrast, the sensitivity is almost the same for the parameters in $(\mathbf{V}_P^2, \mathbf{V}_S^2)$. Furthermore, the condition number of the Hessian matrix is an order of magnitude higher for the $(\boldsymbol{\lambda}, \boldsymbol{\mu})$ parameterization, indicating a poorly-conditioned parameterization. Based on these observations, it is concluded that the $(\mathbf{V}_S^2, \mathbf{V}_P^2)$ parameterization is more stable. This aligns with the observations made by Köhn et al. (2012) and Pan et al. (2018). Therefore, it is chosen as the more reliable parameterization for the subsequent examples.

4.1.3 On the role of Hessian

In order to investigate the role of the Gauss-Newton Hessian matrix ($\mathbf{L}^T\mathbf{L}$) in suppressing inter-parameter cross-talk, we consider the model update equation for the parameterization $(\mathbf{m}_p, \mathbf{m}_s) \equiv (\mathbf{V}_P^2, \mathbf{V}_S^2)$, which can be written as:

$$\mathbf{m}_p = \mathbf{H}_{11}^{-1}\mathbf{g}_x + \mathbf{H}_{12}^{-1}\mathbf{g}_z, \quad (14a)$$

$$\mathbf{m}_s = \mathbf{H}_{21}^{-1}\mathbf{g}_x + \mathbf{H}_{22}^{-1}\mathbf{g}_z, \quad (14b)$$

where \mathbf{H}_{ij}^{-1} represents the blocks of the inverse Hessian matrix and $\mathbf{g} = (\mathbf{g}_x, \mathbf{g}_z)$ is the gradient vector. It is crucial to note that the Hessian blocks \mathbf{H}_{ij}^{-1} are diagonal and amenable to explicit computation. Figure 6 highlights the importance of the Hessian matrix in suppressing parameter cross-talk by demonstrating the influence of each Hessian block in the model update at the 20th iteration. From Figure 6b-c, it can be observed that there is considerable leakage of \mathbf{m}_s into \mathbf{m}_p (marked by black arrows). However, their destructive summation effectively suppresses this leakage. This toy experiment emphasizes the effectiveness of the Hessian in reducing parameter cross-talk during the inversion process. Additionally, the sparsity of the Hessian matrix makes it suitable for large-scale FWI problems.

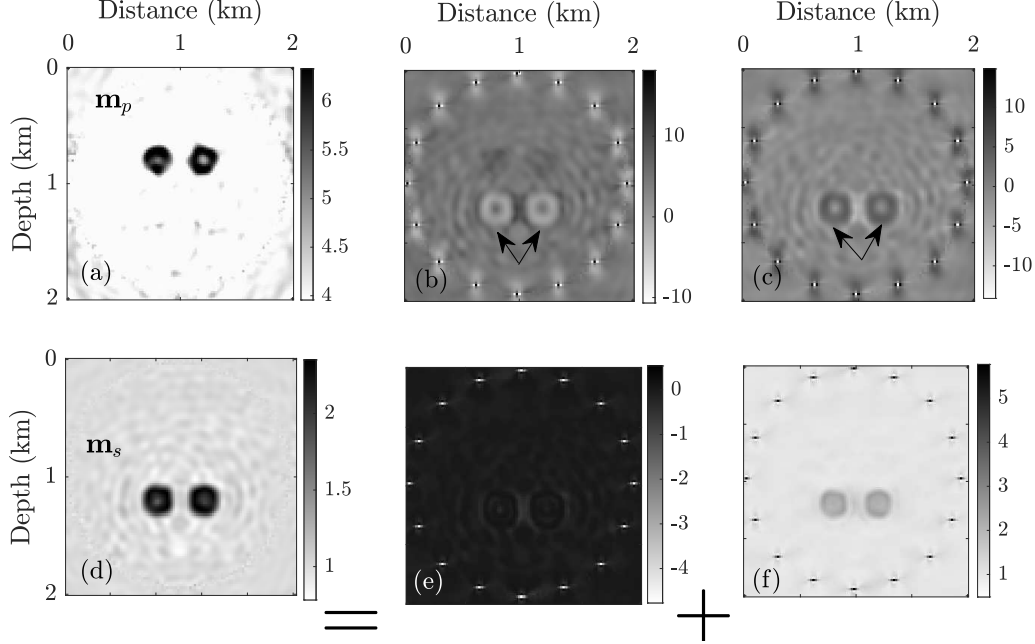


Figure 6: On the role of the Hessian matrix. The model updates for \mathbf{m}_p (a-c) and for \mathbf{m}_s (d-f) at 20th iterations. (a,d) are the total updates which can be decomposed into the parts due to each block of the Hessian; (b,f) diagonal blocks, and (c,e) off diagonal blocks. The diagonal blocks contain dominant features.

4.2 SEG/EAGE overthrust model

In the subsequent experiments, we focus on a 2D section of the 3D SEG/EAGE overthrust \mathbf{V}_P model. The model dimensions are $4.67 \text{ km} \times 20 \text{ km}$ with a grid interval of 25 m. We infer the \mathbf{V}_S model from the \mathbf{V}_P model using an empirical relation proposed by Brocher (2005):

$$\mathbf{V}_S = 0.7858 - 1.2344\mathbf{V}_P + 0.7949\mathbf{V}_P^2 - 0.1238\mathbf{V}_P^3 + 0.0044\mathbf{V}_P^4. \quad (15)$$

This relationship leads to higher values of Poisson’s ratio near the surface, which requires dense spatial sampling in the forward modeling process. To avoid this requirement, we set the minimum value of the \mathbf{V}_S model to be 1.4 km/s (Figure 7a). However, the inversion task remains challenging due to the presence of multiple Poisson’s ratios within the medium. In the context of EFWI, Poisson’s ratio plays a crucial role in influencing the accuracy and stability of the inversion process (Xu and McMechan, 2014; Brossier et al., 2009).

The surface acquisition setup for the inversion process involves 134 sources spaced at intervals of 150 m. Ricker wavelets with dominant frequencies of 10 Hz are used as the source wavelets (\mathbf{b}_x and \mathbf{b}_z). The receivers consist of 401 two-component sensors positioned every 50 m. Absorbing boundary conditions are used on top of the model, unless otherwise stated. The inversion stage begins with models that linearly increase with depth. The \mathbf{V}_S model ranges from 1.2 km/s to 3.8 km/s, while the \mathbf{V}_P model ranges from 2.7 km/s to 6.5 km/s (Figure 7a). The computed Poisson’s ratio and the cross-plot of $\mathbf{m}_s - \mathbf{m}_p$ are shown in Figures 7b and c, respectively. The inversion is carried out in three cycles following the standard multiscale strategy (Bunks et al., 1995), with individual frequencies ranging from 3 Hz to 13 Hz in intervals of 0.5 Hz. The cycles are as follows:

1. Cycle 1: Frequencies range from 3 Hz to 6 Hz.
2. Cycle 2: Frequencies range from 3 Hz to 7.5 Hz.
3. Cycle 3: Frequencies range from 3 Hz to 13 Hz.

The inversion process consists of 20 iterations for the first frequency component and 10 iterations for the subsequent frequencies, resulting in a total of 410 iterations. A fixed penalty parameter of $\beta = 10^6$ is used throughout the inversion process. First, we conducted a comparative analysis to assess the efficacy of the proposed method against traditional FWI. The evaluation focused on a specific segment of the SEG/EAGE overthrust model, demarcated by a rectangle in Figure 7a. Two distinct starting models were utilized: one derived by smoothing the original models (shown at the top of Figure 8), and the other featuring linear depth-dependent increments, as illustrated at the top of Figure 9.

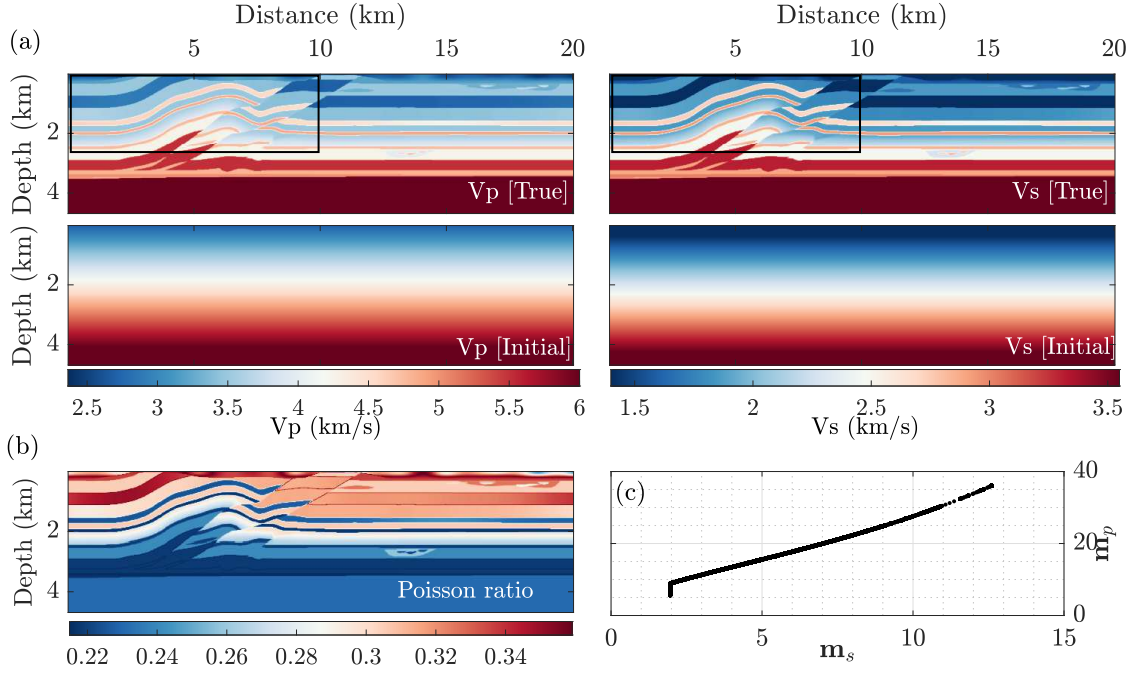


Figure 7: (a) True and initial P- and S-wave velocity models, (b) Poisson's ratio, and (c) cross-plot of m_p versus m_s .

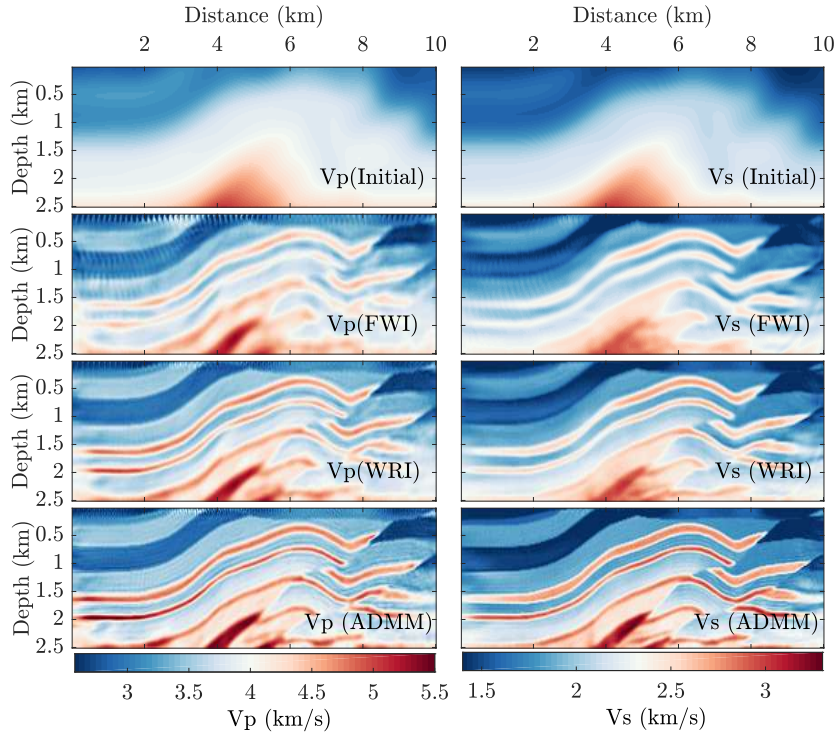


Figure 8: Comparison between classic FWI, WRI and ADMM for the case of smooth initial models.

Three inversion methods were employed: classical FWI based on the reduced formulation, the proposed algorithm

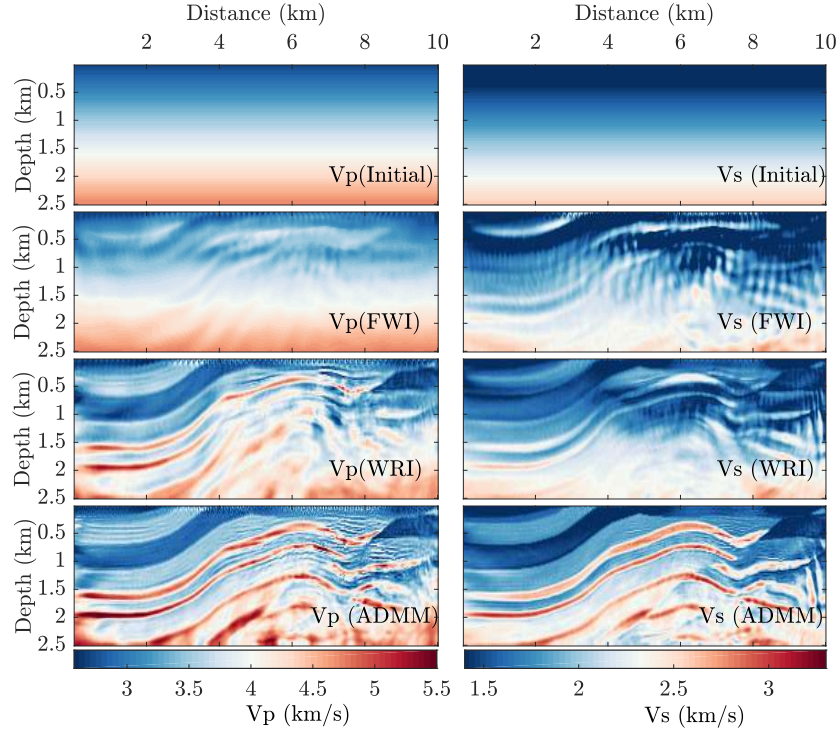


Figure 9: Comparison between classic FWI, WRI and ADMM for the case of linearly increased initial model.

leveraging ADMM, and WRI, where WRI was applied with Lagrange multipliers set to zero. Figure 8 shows the inversion results from the smooth initial models, with representations of initial models and reconstructed models for classical FWI, WRI, and ADMM displayed from top to bottom, respectively. Given the accuracy of the initial models, all three methods successfully converged to the true solution. Notably, the use of WRI and ADMM techniques led to enhanced resolution in the inverted models, with the ADMM exhibiting superior accuracy. However, a substantial shift in the quality of estimated models occurred when using a less accurate starting model (Figure 9). Classic FWI became trapped in a local minimum, failing to reconstruct both V_P and V_S models. Conversely, the WRI approach improved reconstruction, although the V_S model still exhibited artifacts. Remarkably, the ADMM methodology outperformed other approaches, demonstrating superior performance. Quantitative validation of these observations is presented in Figure 10, where subfigures a and b illustrate the model error curves for V_P and V_S models with smoothed initial models. Subfigures c and d depict similar curves for cases with linearly increased initial models. These model error curves underscore the significant convergence rate of the ADMM technique for both scenarios.

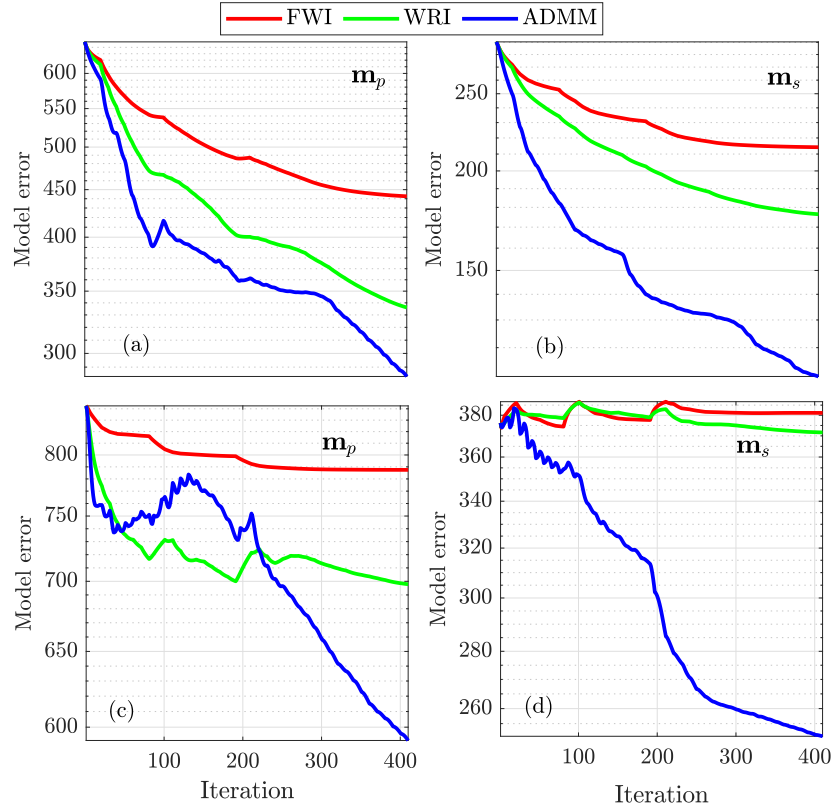


Figure 10: Evolution of the model error versus iteration for classic FWI, WRI and ADMM started with (a,b) smooth initial models (Figure 8) and (c,d) linearly increased initial models (Figure 9).

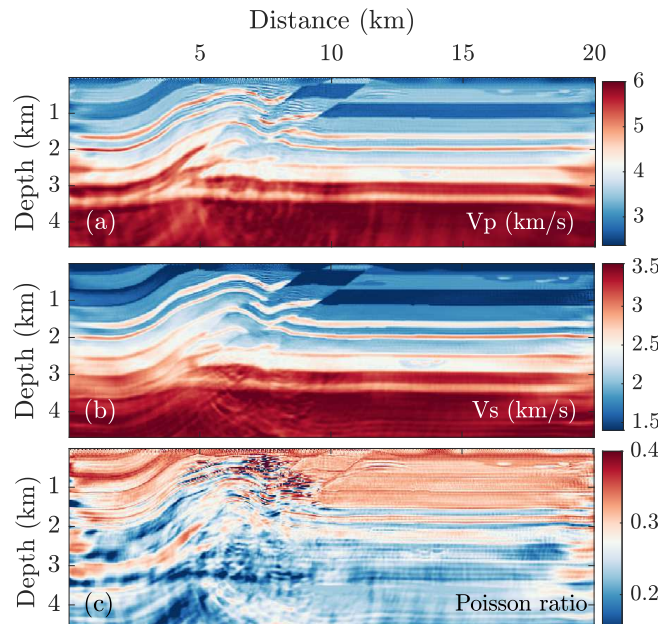


Figure 11: Estimated (a) V_p , (b) V_s , and (c) Poisson ratio using squared velocity parametrization.

4.2.1 Elastic FWI with ADMM

We continued the investigation for EFWI using the ADMM method and investigated several characteristics to increase its performance. The inversion was performed to reconstruct models shown in Figure 7a. Figures 11a and b show the final inversion results for the V_p and V_s models, respectively. Figure 11c displays the computed Poisson's ratio for the final estimated models. To evaluate the performance of the method, Figure 12 compares the extracted velocity profiles at various locations. The suggested method demonstrates good accuracy in reconstructing the models. Figure 13

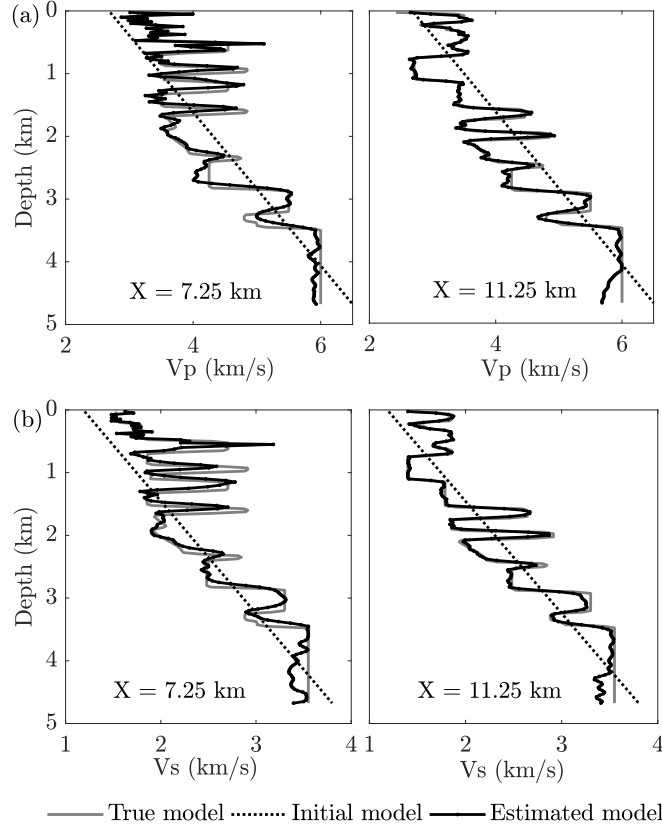


Figure 12: Comparison between vertical velocity profiles at different locations labeled by X for (a) V_p model and (b) V_s model.

illustrates the convergence curves associated with the inversion process over the iterations. The figure clearly illustrates the decrease in errors for each frequency component throughout the iterations. It is noteworthy that, due to the distinct nature of the problems solved for each frequency, there might be instances of error increase during the transition from one frequency to another in the inversion process. In Figure 14 synthetic seismograms (horizontal and vertical components) are computed in the initial, true and estimated models to evaluate the fit of the phase and amplitude data and to determine the accuracy of the velocity reconstruction. To determine if the initial and true models were affected by cycle skipping, we superimpose the seismograms computed in the initial and estimated models (in red) over those computed in the true model (in blue). It can be seen that seismograms computed in the initial models are cycle skipped. However, a very good match between seismograms computed in true and estimated models are obtained. In the subsequent sections, we will explore the influence of various factors and assess the effectiveness of the algorithm.

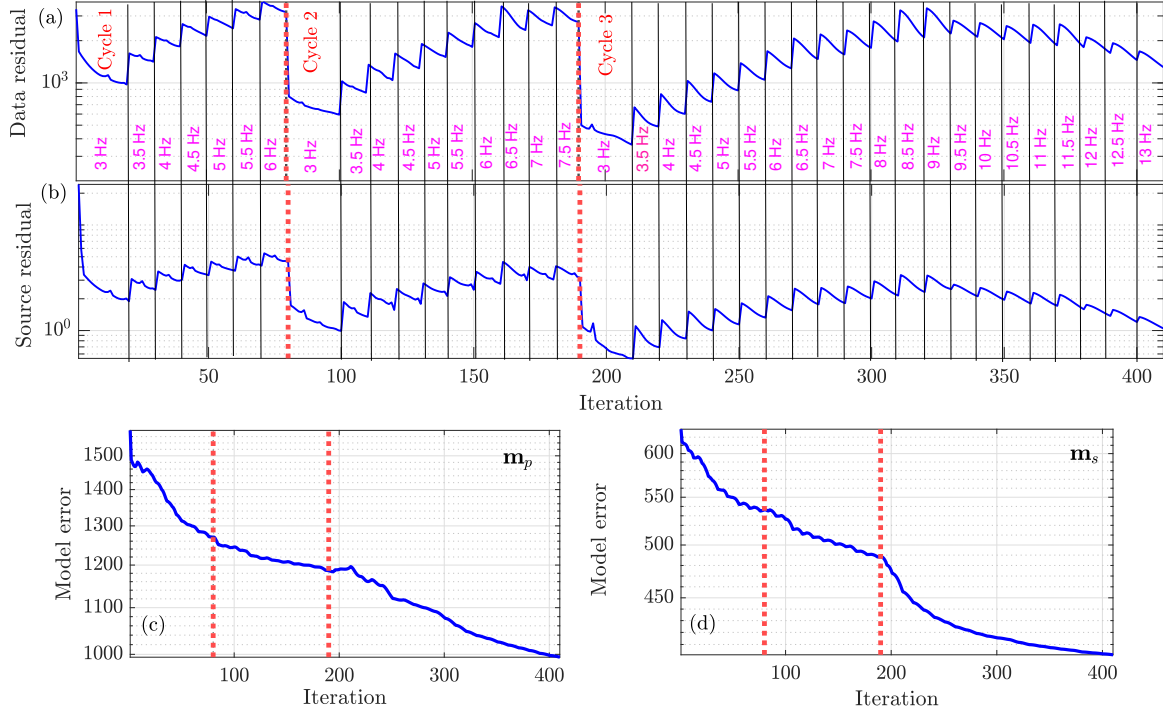


Figure 13: Evolution of the (a) data residual, (b) source residual, (c) m_p model error, and (d) m_s model error versus inversion iteration.

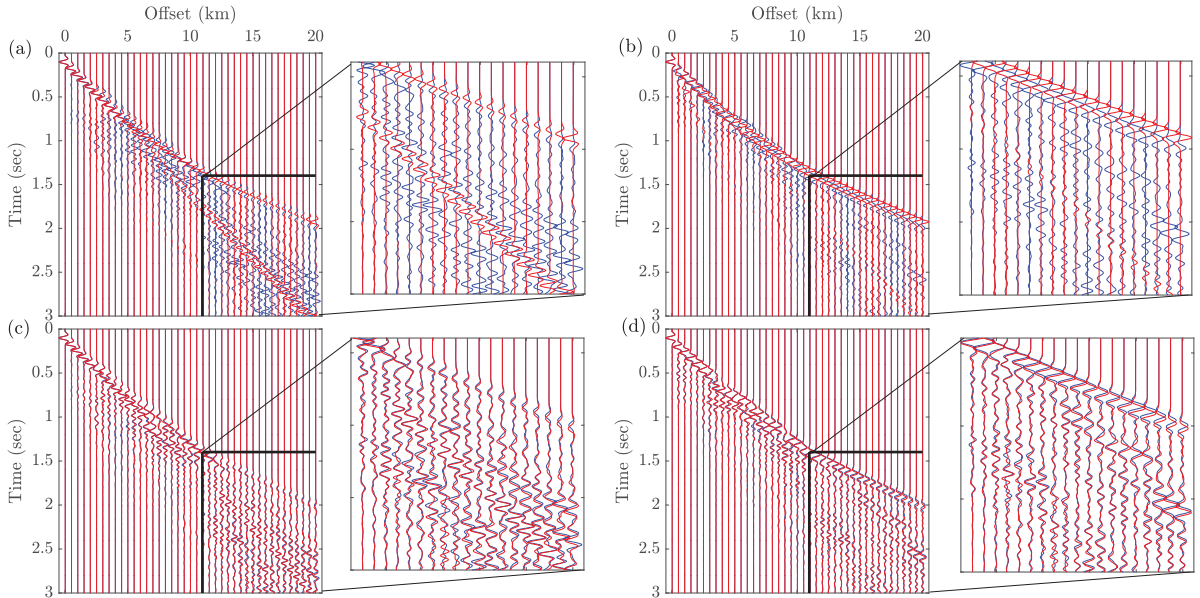


Figure 14: Direct comparison of synthetic seismograms is shown in (a) and (c) for the horizontal component, and in (b) and (d) for the vertical component. Panels (a) and (b) show the seismograms computed from the true model (blue), overlays in a red wiggle plot representing the seismograms computed from the initial model. Panels (c) and (d) show the seismograms computed from the inverted model, also with overlays.

4.2.2 The role of damping Lagrange multipliers

In order to address the issue of slow convergence caused by an inaccurate initial model, we applied damping to the Lagrange multiplier update in the early iterations of the ADMM algorithm. We tested various damping parameters (ξ) of 1, 1.5, 2, 2.5, 3, and 4, as described in equation 13. The performance of the ADMM iterations was evaluated based on the computed source residual, data residual, and model error over iterations. The quantitative analysis results are presented in Figure 15. The findings indicate that damping has a significant positive impact on the convergence of the algorithm, particularly for damping values of $\xi = 2.5, 3,$ and 4 . After considering these results, we selected a damping value of $\xi = 4$ for the subsequent experiments.

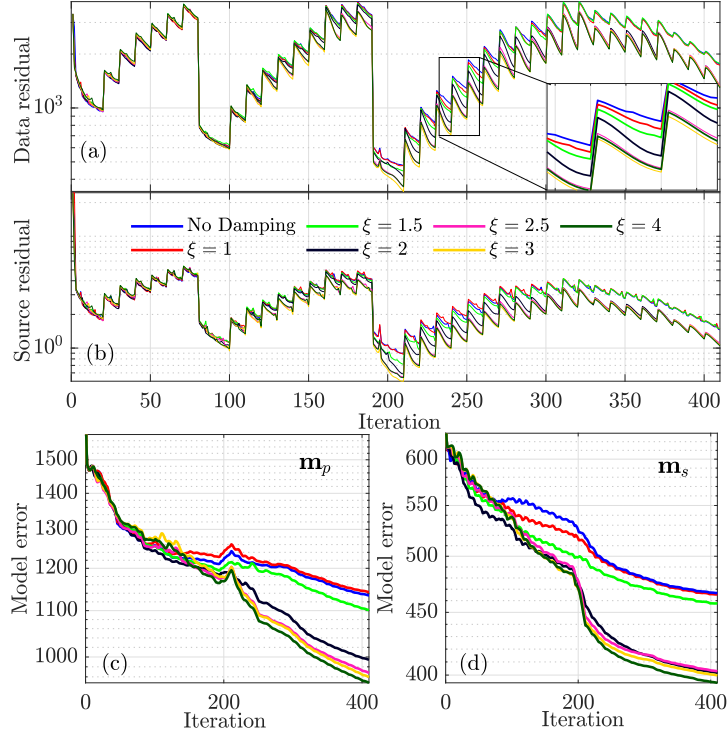


Figure 15: The effect of the damping multipliers on the stability of the ADMM iterations (equation 13) using different values of ξ . Evolution over iteration of data residual (a), source residual (b), m_p model error (c) and m_s model error (d).

4.2.3 The role of penalty parameter

To assess the performance of the algorithm with different penalty parameter values, we conducted a test using values ranging from $\beta = 10^2$ to $\beta = 10^{10}$. We compared the evolution of the data residual, source residual, and model error for different values of β , as shown in Figure 16. The results indicate that when the value of β is too low ($\beta < 10^4$), the algorithm places more emphasis on minimizing the data term $\|\mathbf{P}\mathbf{u} - \mathbf{d}\|_2^2$. On the other hand, for large values of β ($\beta > 10^7$), the source term is given more weight. In both cases, the algorithm fails to produce satisfactory results. However, penalty parameter values in the range of $\beta \in (10^4, 10^7)$ yielded satisfactory performance, balancing the influence of both the data and source terms.

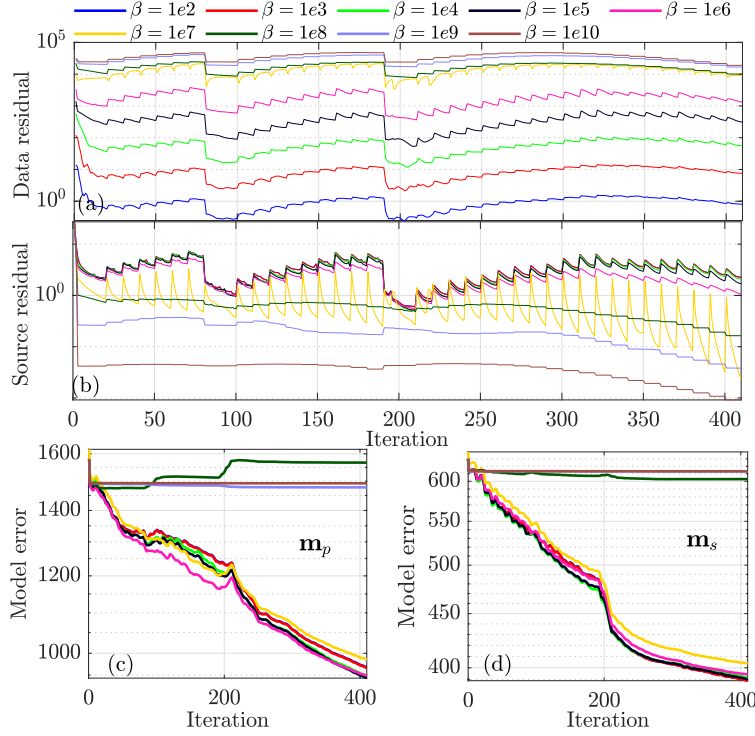


Figure 16: On the choice of the penalty parameter: The performance of the AL based EFWI with different (fixed) values of the penalty parameter (β). Evolution over iteration of data residual (a), source residual (b), m_p model error (c) and m_s model error (d).

4.2.4 Inversion of noise-contaminated data

In order to assess the effectiveness of our method in the presence of noise, we conducted an experiment using noisy data. Gaussian distributed random noise with a signal-to-noise ratio (S/R) of 10 dB was added to the data. For a frequency component of 7.5 Hz, Figure 17 provides a comparison between the noise-free data and the noisy data in the source-receiver coordinate. Despite the added noise, the main features of the data are still preserved. We then performed the inversion using the same setup, but with the noisy data. The resulting V_p and V_s models are displayed in Figure 18b. It can be observed that the impact of noise on the inversion results is not significant when compared to the results obtained from the noise-free data (Figure 18a). This suggests that our method is relatively robust to noise and can produce reliable inversion results even in the presence of noise.

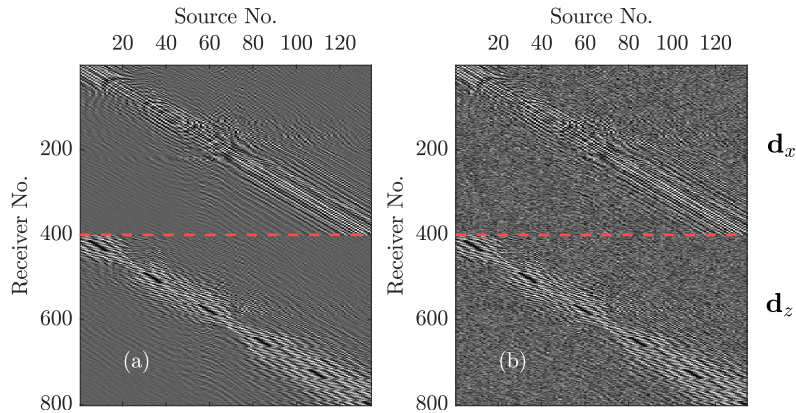


Figure 17: Comparison between (a) noise-free and (b) noise contaminated 7.5 Hz data with S/R of 10 dB. The dashed red line separates horizontal and vertical components of the receivers.

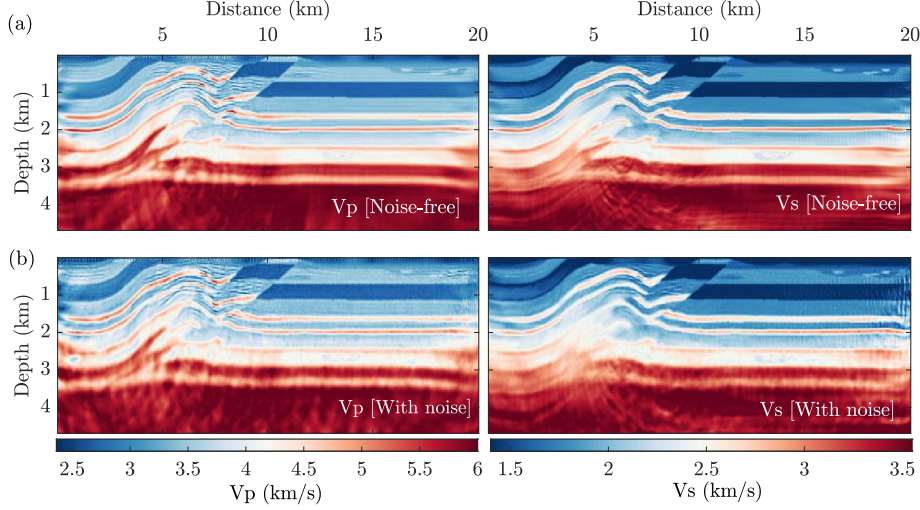


Figure 18: Inversion results obtained from (a) noise-free data and (b) noisy data.

4.2.5 The role of multi-physical constraints

In this subsection, we conducted experiments to test the impact of implementing physical constraints on the inversion results. We constructed two sets, C_1 and C_2 , based on the true models (Figure 19). C_1 was constructed based on the lowest and highest values of the true models (represented by dashed lines), while C_2 was constructed based on the cross-plot of V_p and V_s logs at $X = 2.5$ km (represented by black dots). We tested two cases: projection onto C_1 and projection onto $C_1 \cap C_2$. The inverted results for these cases are shown in Figure 20a, b, d, and e. To assess the quality of the estimates, we also plotted the Poisson’s ratio residual sections. It can be observed that when we implemented the constraint $\mathbf{m} \in C_1 \cap C_2$, the quality of the results significantly improved (Figure 20f versus c), especially in the faulted zone indicated by the black rectangle. This improvement is further supported by the cross-plots shown in Figure 21a, b, as well as the evolution of the model errors over the iterations in Figure 21c, d. These results demonstrate that incorporating physical constraints into the inversion process, such as constraining the model to lie within the intersection of multiple convex sets, can greatly enhance the accuracy and reliability of the inversion results.

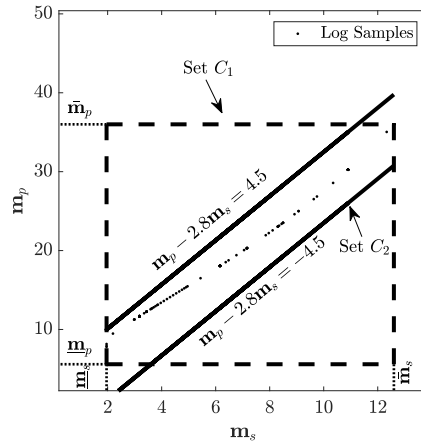


Figure 19: Elastic FWI with physical constraints: $(\mathbf{m}_s - \mathbf{m}_p)$ cross-plot (the black-dots) for a true vertical profile and two closed-convex sets (C_1 and C_2) defined as the physical constraints according to vertical velocity log samples.

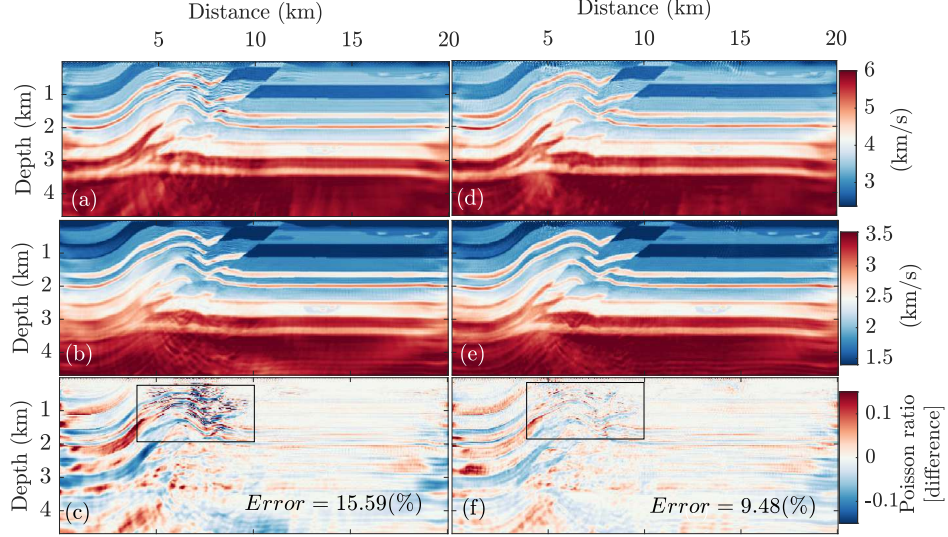


Figure 20: Inversion with physical constraints. The (a) estimated V_p , (b) estimated V_s , and (c) difference between true and estimated Poisson's ratio when forcing $\mathbf{m} \in C_1$. (d-f) same as (a-c) for the case forcing $\mathbf{m} \in C_1 \cap C_2$.

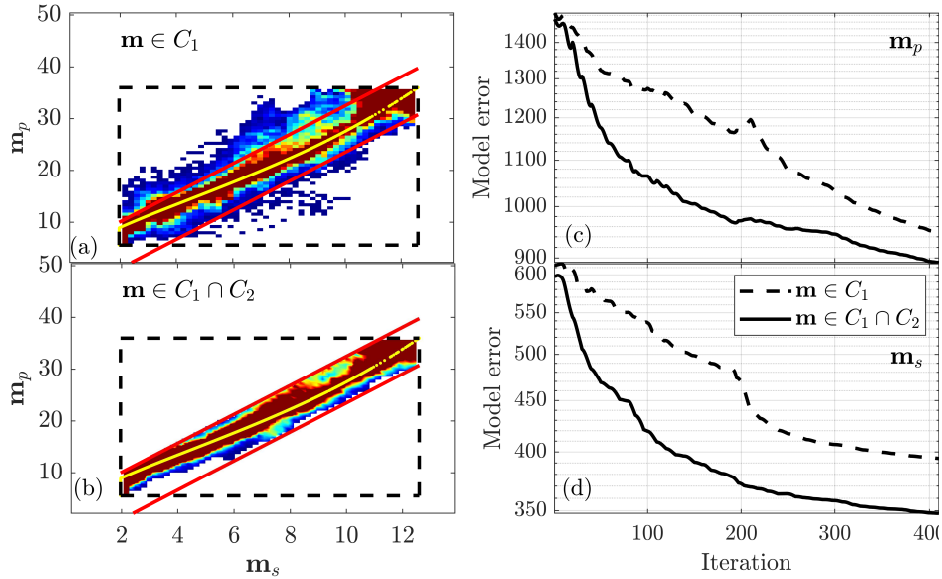


Figure 21: Inversion with physical constraints. (a) Cross plot of m_p (Figure 20a) versus m_s (Figure 20b) obtained by forcing $\mathbf{m} \in C_1$. (b) Cross plot of m_p (Figure 20d) versus m_s (Figure 20e) obtained by forcing $\mathbf{m} \in C_1 \cap C_2$, where the yellow curve indicates the true cross plot. The evolution of model errors over iteration for (c) m_p and (d) m_s .

4.2.6 Inversion with source sketching

In order to address the computational burden associated with solving the PDE in the ADMM iteration, we propose the use of source sketching, a method based on randomized discrete cosine transform (DCT) as the sketching matrix. The theoretical background of this method can be found in (Aghazade et al., 2021).

To assess the performance of the source sketching method, we conducted a series of experiments with different numbers of sketched sources. The total number of physical sources in the inversion was 134, and a total of 410 iterations were performed. During the initial 20 iterations, we used 50 sketched sources instead of the full set of 134 sources.

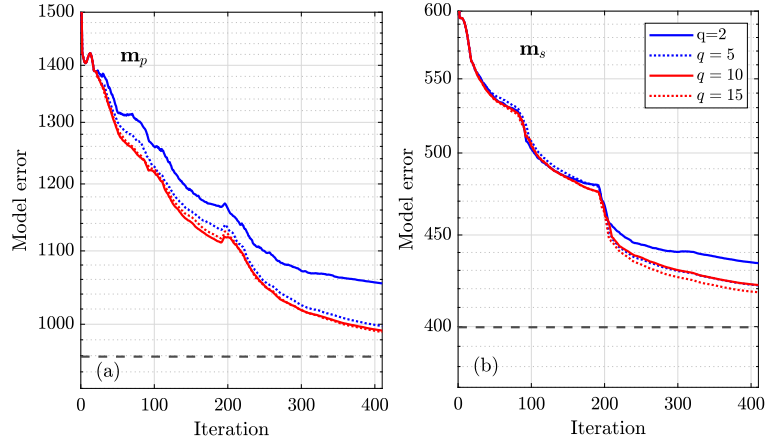


Figure 22: Elastic FWI with source sketching: The evolution of the model error during iteration using different sketched sources for (a) \mathbf{m}_p and (b) \mathbf{m}_s . The inversion is initialized with 50 sketched sources up to 20 iterations followed by sketched sources of $q = 2, 5, 10, 15$. The horizontal dashed line indicates the final model error obtained by the full source inversion (134 sources).

For the remaining 390 iterations, we conducted experiments with different numbers of sketched sources: $q=2, 5, 10$, and 15. The evolution of the model error for each experiment is shown in Figure 22. The horizontal dashed line represents the final model error achieved through full-source (134 sources) inversion. In terms of accuracy, we observed that as the number of sketched sources increased, the final inversion results approached those obtained with the full set of sources. Regarding computational efficiency, the number of PDEs solved was significantly reduced compared with full-source inversion: from 54940 for the full set of sources to 1780 ($q = 2$), 2950 ($q = 5$), 4900 ($q = 10$), and 6850 ($q = 15$) for the sketched sources. Excluding the first 20 iterations, the computation speed-up, measured as $(1 - q/134) \times 100$, was approximately 98.5% ($q = 2$), 96.2% ($q = 5$), 92.5% ($q = 10$), and 88.8% ($q = 15$), indicating the efficiency of the source sketching method.

4.2.7 Inversion with free surface effects

In this subsection, we investigate the impact of free surface effects on the accurate estimation of subsurface properties in EFWI. It is well-known that free surface effects can compromise the reliability of the inversion process (Brossier et al., 2009). To illustrate this, we compare computed seismograms with and without free surface effects in Figures 23a-23d, respectively. The presence of high-energy free surface effects introduces additional nonlinearities to the problem, making the inversion more challenging. We initiated the inversion process with 1D initial models, as shown in Figure 7a, and the final inversion results as well as estimated Poisson's ratio, are displayed in Figure 24a-c. Comparing these results with the ones obtained using absorbing boundary conditions on the surface (Figure 11), it is evident that the presence of free surface effects has degraded the quality of the estimates. This degradation is further demonstrated by comparing the convergence curves associated with the inversion process, as shown in Figures 25 and 13. Overall, these findings highlight the importance of accounting for free surface effects in EFWI and the challenges they pose in accurately estimating subsurface properties.

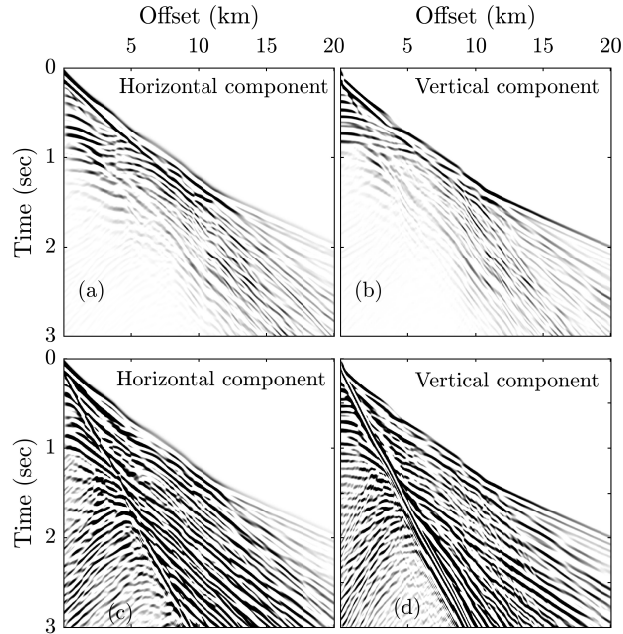


Figure 23: Comparison between true seismograms computed (a-b) without and (c-d) with free surface effects.

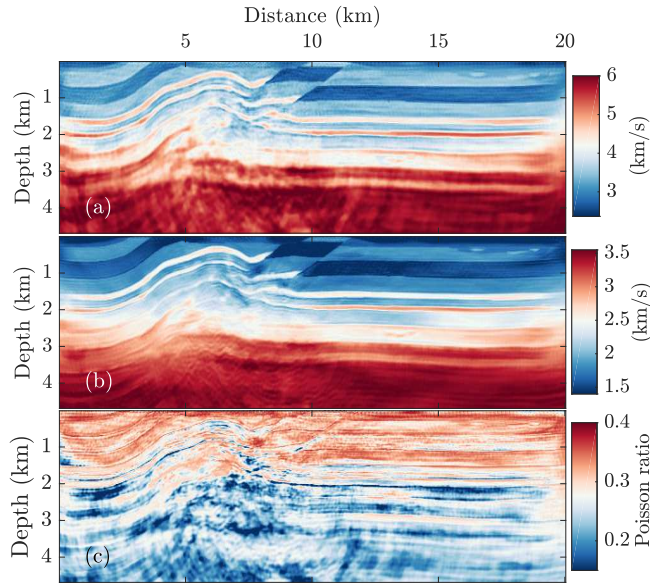


Figure 24: Inversion with free surface effects. The (a) estimated V_p model, (b) estimated V_s model, and (c) Estimated Poisson's ratio. The inversion was performed by forcing $\mathbf{m} \in C_1 \cap C_2$ and using the 1D initial models in Figure 7.

5 Conclusions

We have introduced a new elastic full-waveform inversion (EFWI) algorithm, leveraging the ADMM and reconstructed wavefields. This innovative approach addresses the intricate task of accurate subsurface property estimation with notable advantages. The algorithm stands out for its inherent flexibility, accommodating physical constraints, and efficient implementation of the Hessian matrix through ADMM, mitigating interparameter cross-talk. A key strength lies in its freedom from step length tuning, simplifying the implementation process. Extensive numerical experiments provided underscore the algorithm's effectiveness, showcasing superior convergence properties and stability compared

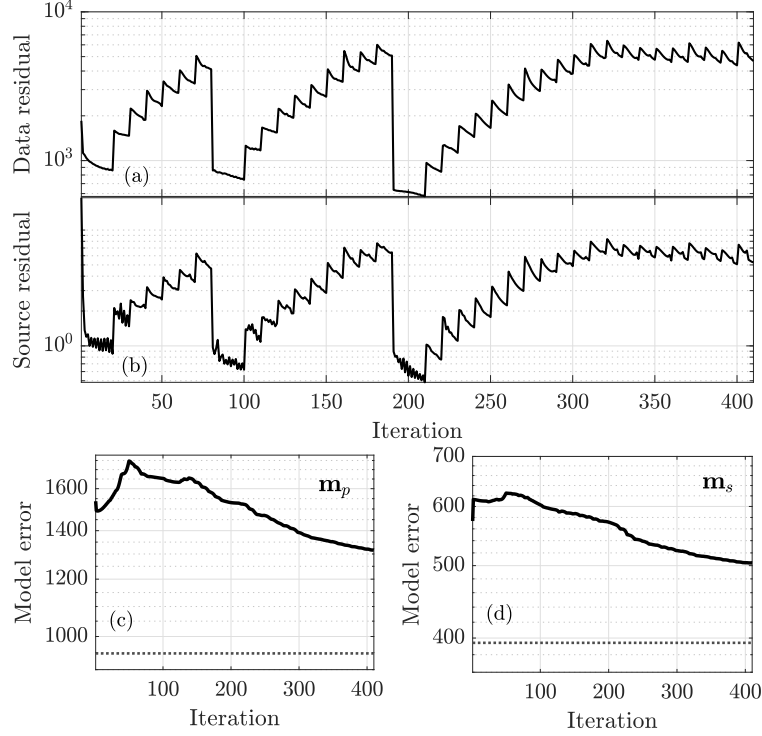


Figure 25: Inversion with free surface effects. The variation with iteration associated to (a) data residual, (b) source residual, (c) \mathbf{m}_p model error, and (d) \mathbf{m}_s model error. The horizontal dashed line represents the final model error achieved without free surface effects.

with the classical FWI. Notably, it exhibited robustness against rough initial models, noise, and free surface effects, ensuring reliable inversion results. We have investigated the role of the Hessian matrix in suppressing cross-talk and the application of randomized source sketching for enhanced efficiency. Although regularization was not implemented in this study, the algorithm's inherent flexibility allows for the straightforward incorporation of regularization techniques, empowering users with greater control over the inversion process.

6 ACKNOWLEDGMENTS

This research was partially funded by the SONATA BIS (grant no. 2022/46/E/ST10/00266) of the National Science Center in Poland.

7 DATA AND MATERIALS AVAILABILITY

Data associated with this research are available and can be obtained by contacting the corresponding author.

Appendix A: Model update for $(\mathbf{V}_P, \mathbf{V}_S)$

The optimization over $(\mathbf{V}_P, \mathbf{V}_S)$ will be nonlinear thus we update the parameters by using the Gauss-Newton algorithm as

$$\mathbf{m}^{k+1} = \mathbf{m}^k + \alpha^k \delta \mathbf{m}^k, \quad (16)$$

where α^k is the step-length and $\delta \mathbf{m}$ is the step direction, satisfying

$$\mathbf{H}^k \delta \mathbf{m}^k = -\mathbf{g}^k, \quad (17)$$

where \mathbf{g}^k and \mathbf{H}^k are the gradient and the Hessian of the AL function $\mathcal{L}_\beta(\mathbf{u}^{k+1}, \mathbf{m}, \mathbf{s}^k)$ defined as:

$$\mathbf{g}^k = [(\partial_{\mathbf{m}} \mathbf{A}) \mathbf{u}^{k+1}]^T [\mathbf{A} \mathbf{u}^{k+1} - \mathbf{b} - \mathbf{s}^k], \quad (18a)$$

$$\mathbf{H}^k = [(\partial_{\mathbf{m}} \mathbf{A}) \mathbf{u}^{k+1}]^T [(\partial_{\mathbf{m}} \mathbf{A}) \mathbf{u}^{k+1}], \quad (18b)$$

where $\mathbf{A} \equiv \mathbf{A}(\mathbf{m}^k)$. Here the required term is computing $\partial_{\mathbf{m}} \mathbf{A}$, which is:

$$\partial_{\mathbf{m}} \mathbf{A} = \begin{bmatrix} \partial_{\mathbf{V}_P} \mathbf{A}_x & \partial_{\mathbf{V}_S} \mathbf{A}_x \\ \partial_{\mathbf{V}_P} \mathbf{A}_z & \partial_{\mathbf{V}_S} \mathbf{A}_z \end{bmatrix} \quad (19)$$

where:

$$\begin{aligned} \partial_{\mathbf{V}_P} \mathbf{A}_x &= 2 \left[\text{diag} \left(\partial_{xx} \circ (\boldsymbol{\rho} \circ \mathbf{V}_P^k) \right) + \text{diag} \left(\partial_{xz} \circ (\boldsymbol{\rho} \circ \mathbf{V}_P^k) \right) \right], \\ \partial_{\mathbf{V}_S} \mathbf{A}_x &= 2 \left[\text{diag} \left(\partial_{zz} \circ (\boldsymbol{\rho} \circ \mathbf{V}_S^k) \right) - \text{diag} \left(\partial_{xz} \circ (\boldsymbol{\rho} \circ \mathbf{V}_S^k) \right) \right], \\ \partial_{\mathbf{V}_P} \mathbf{A}_z &= 2 \left[\text{diag} \left(\partial_{zz} \circ (\boldsymbol{\rho} \circ \mathbf{V}_P^k) \right) + \text{diag} \left(\partial_{xz} \circ (\boldsymbol{\rho} \circ \mathbf{V}_P^k) \right) \right], \\ \partial_{\mathbf{V}_S} \mathbf{A}_z &= 2 \left[\text{diag} \left(\partial_{xx} \circ (\boldsymbol{\rho} \circ \mathbf{V}_S^k) \right) - \text{diag} \left(\partial_{xz} \circ (\boldsymbol{\rho} \circ \mathbf{V}_S^k) \right) \right]. \end{aligned} \quad (20)$$

Appendix B: Projection onto intersection of two convex sets by ADMM

Given two closed convex sets C_1 and C_2 , the model update step in equation 8b requires solving

$$\min_{\mathbf{m}} \|\mathbf{L}\mathbf{m} - \mathbf{y}\|_2^2 \quad \text{s.t.} \quad \mathbf{m} \in C_1 \cap C_2. \quad (21)$$

The constrained problem described above can be expressed as an equivalent optimization problem:

$$\min_{\mathbf{m}} \|\mathbf{L}\mathbf{m} - \mathbf{y}\|_2^2 + I_C(\mathbf{m}), \quad (22)$$

where C is the intersection of two sets C_1 and C_2 , denoted by $C_1 \cap C_2$, and $I_C(\mathbf{m})$ represent the indicator function of C :

$$I_C(\mathbf{m}) = \begin{cases} 0 & \text{if } \mathbf{m} \in C \\ \infty & \text{if } \mathbf{m} \notin C. \end{cases} \quad (23)$$

Including the indicator functions guarantee that any candidate solution \mathbf{m} that is not in C will have an infinite objective value, making it infeasible. To solve 22, we split the two terms of the objective function by introducing auxiliary variables \mathbf{p} and constraint $\mathbf{m} = \mathbf{p}$:

$$\min_{\mathbf{m}, \mathbf{p}} \|\mathbf{L}\mathbf{m} - \mathbf{y}\|_2^2 + I_C(\mathbf{p}) \quad \text{s.t.} \quad \mathbf{m} - \mathbf{p} = 0. \quad (24)$$

The ADMM algorithm solves this constrained problem by the following iteration:

$$\mathbf{m}^{k+1} = (\mathbf{L}^T \mathbf{L} + \gamma \mathbf{I})^{-1} (\mathbf{L}^T \mathbf{y} + \gamma (\mathbf{p}^k + \mathbf{q}^k)), \quad (25a)$$

$$\mathbf{p}^{k+1} = \mathbf{P}_C(\mathbf{m}^{k+1} - \mathbf{q}^k), \quad (25b)$$

$$\mathbf{q}^{k+1} = \mathbf{q}^k + \mathbf{p}^{k+1} - \mathbf{m}^{k+1}, \quad (25c)$$

where \mathbf{q} is the scaled dual variable, $\gamma > 0$ is the penalty parameter, and \mathbf{P}_C is the projection operators onto C .

References

- Aghamiry, H. S., A. Gholami, and S. Operto, 2019, Improving full-waveform inversion by wavefield reconstruction with the alternating direction method of multipliers: *Geophysics*, **84**, R139–R162.
- , 2020, Multiparameter wavefield reconstruction inversion for wavespeed and attenuation with bound constraints and total variation regularization: *Geophysics*, **85**, R381–R396.
- Aghazade, K., H. S. Aghamiry, A. Gholami, and S. Operto, 2021, Randomized source sketching for full waveform inversion: *IEEE Transactions on Geoscience and Remote Sensing*, **60**, 1–12.
- Barnes, C., and M. Charara, 2008, Full-waveform inversion results when using acoustic approximation instead of elastic medium: *SEG Technical Program Expanded Abstracts*, **27**, 1895–1899.
- , 2009, The domain of applicability of acoustic full-waveform inversion for marine seismic data: *Geophysics*, **74**, WCC91–WCC103.
- Baumstein, A., 2013, POCS-based geophysical constraints in multi-parameter full wavefield inversion: *75th EAGE Conference & Exhibition incorporating SPE EUROPEC 2013*, European Association of Geoscientists & Engineers, cp-348.
- Borisov, D., R. D. Miller, S. L. Peterie, J. Ivanov, A. M. Hoch, and S. D. Sloan, 2022, Graph-space optimal transport-based 3D elastic FWI for near-surface seismic applications: *Second International Meeting for Applied Geoscience & Energy*, Society of Exploration Geophysicists and American Association of Petroleum, 2153–2157.
- Borisov, D., A. Stopin, and R. Plessix, 2014, Acoustic pseudo-density full waveform inversion in the presence of hard thin beds: *76th EAGE Conference and Exhibition 2014*, EAGE Publications BV, 1–5.
- Boyd, S., N. Parikh, and E. Chu, 2011, *Distributed optimization and statistical learning via the alternating direction method of multipliers*: Now Publishers Inc.
- Brocher, T. M., 2005, Empirical relations between elastic wavespeeds and density in the Earth’s crust: *Bulletin of the seismological Society of America*, **95**, 2081–2092.
- Brossier, R., S. Operto, and J. Virieux, 2009, Seismic imaging of complex onshore structures by 2D elastic frequency-domain full-waveform inversion: *Geophysics*, **74**, WCC105–WCC118.
- Bunks, C., F. M. Saleck, S. Zaleski, and G. Chavent, 1995, Multiscale seismic waveform inversion: *Geophysics*, **60**, 1457–1473.
- Chen, G., W. Yang, H. Wang, H. Zhou, and X. Huang, 2022, Elastic full waveform inversion based on full-band seismic data reconstructed by dual deconvolution: *IEEE Geoscience and Remote Sensing Letters*, **19**, 1–5.
- Chen, J.-B., and J. Cao, 2016, Modeling of frequency-domain elastic-wave equation with an average-derivative optimal method: *Geophysics*, **81**, T339–T356.
- Chi, B., L. Dong, and Y. Liu, 2014, Full waveform inversion method using envelope objective function without low frequency data: *Journal of Applied Geophysics*, **109**, 36–46.
- Choi, Y., D.-J. Min, and C. Shin, 2008, Frequency-domain elastic full waveform inversion using the new pseudo-Hessian matrix: Experience of elastic Marmousi-2 synthetic data: *Bulletin of the Seismological Society of America*, **98**, 2402–2415.
- Duan, Y., and P. Sava, 2016, Elastic wavefield tomography with physical model constraints: *Geophysics*, **81**, R447–R456.
- Dykstra, R. L., 1983, An algorithm for restricted least squares regression: *Journal of the American Statistical Association*, **78**, 837–842.
- Forgues, E., and G. Lambaré, 1997, Parameterization study for acoustic and elastic ray+Born inversion: *Journal of Seismic Exploration*, **6**, 253–278.
- Gabay, D., and B. Mercier, 1976, A dual algorithm for the solution of nonlinear variational problems via finite element approximation: *Computers & mathematics with applications*, **2**, 17–40.
- Gauthier, O., J. Virieux, and A. Tarantola, 1986, Two-dimensional nonlinear inversion of seismic waveform : numerical results: *Geophysics*, **51**, 1387–1403.
- Gholami, A., 2023, Full waveform inversion and Lagrange multipliers: arXiv preprint [arXiv:2311.11010](https://arxiv.org/abs/2311.11010).
- Gholami, A., H. S. Aghamiry, and S. Operto, 2022, Extended-space full-waveform inversion in the time domain with the augmented Lagrangian method: *Geophysics*, **87**, R63–R77.
- , 2023, Multiplier waveform inversion (MWI): A reduced-space FWI by the method of multipliers: *Geophysics*, **88**, 1–60.
- Gholami, Y., R. Brossier, S. Operto, A. Ribodetti, and J. Virieux, 2013, Which parametrization is suitable for acoustic VTI full waveform inversion? - Part 1: sensitivity and trade-off analysis: *Geophysics*, **78**, R81–R105.
- Haber, E., U. M. Ascher, and D. Oldenburg, 2000, On optimization techniques for solving nonlinear inverse problems: *Inverse problems*, **16**, 1263.
- Hu, Y., L.-Y. Fu, Q. Li, W. Deng, and L. Han, 2022, Frequency-wavenumber domain elastic full waveform inversion with a multistage phase correction: *Remote Sensing*, **14**, 5916.

- Jun, H., Y. Kim, J. Shin, C. Shin, and D.-J. Min, 2014, Laplace-Fourier-domain elastic full-waveform inversion using time-domain modeling: *Geophysics*, **79**, R195–R208.
- Kazei, V., and T. Alkhalifah, 2019, Scattering radiation pattern atlas: What anisotropic elastic properties can body waves resolve?: *Journal of Geophysical Research: Solid Earth*, **124**, 2781–2811.
- Köhn, D., D. De Nil, A. Kurzman, A. Przebindowska, and T. Bohlen, 2012, On the influence of model parametrization in elastic full waveform tomography: *Geophysical Journal International*, **191**, 325–345.
- Kwon, J., H. Jun, H. Song, U. G. Jang, and C. Shin, 2017, Waveform inversion in the shifted Laplace domain: *Geophysical Journal International*, **210**, 340–353.
- Li, Y. E., and L. Demanet, 2015, Phase and amplitude tracking for seismic event separation: *Geophysics*, **80**, WD59–WD72.
- Lin, Y., and L. Huang, 2014, Acoustic-and elastic-waveform inversion using a modified total-variation regularization scheme: *Geophysical Journal International*, **200**, 489–502.
- Marty, P., C. Boehm, and A. Fichtner, 2022, Elastic full-waveform inversion for transcranial ultrasound computed tomography using optimal transport: *IEEE International Ultrasonics Symposium (IUS)*, IEEE, 1–4.
- Métivier, L., R. Brossier, S. Operto, and J. Virieux, 2014, Multi-parameter FWI-an illustration of the Hessian operator role for mitigating trade-off between parameter classes: 6th EAGE Saint Petersburg International Conference and Exhibition, 1–5.
- Mora, P. R., 1988, Elastic wavefield inversion of reflection and transmission data: *Geophysics*, **53**, 750–759.
- Mulder, W., and R. E. Plessix, 2008, Exploring some issues in acoustic full waveform inversion: *Geophysical Prospecting*, **56**, 827–841.
- Nocedal, J., and S. Wright, 2006, Numerical optimization: Springer Science & Business Media.
- Operto, S., A. Gholami, H. S. Aghamiry, G. Guo, F. Mamfoumbi, S. Beller, K. Aghazade, F. Mamfoumbi, L. Combe, and A. Ribodetti, 2023, Extending the search space of full-waveform inversion beyond the single-scattering born approximation: A tutorial review: *Geophysics*, **88**, 1–32.
- Operto, S., Y. Gholami, V. Prioux, A. Ribodetti, R. Brossier, L. Metivier, and J. Virieux, 2013, A guided tour of multiparameter full-waveform inversion with multicomponent data: From theory to practice: *The leading edge*, **32**, 1040–1054.
- Operto, S., J. Virieux, J. X. Dessa, and G. Pascal, 2006, Crustal imaging from multifold ocean bottom seismometers data by frequency-domain full-waveform tomography: application to the eastern Nankai trough: *Journal of Geophysical Research*, **111**.
- Pan, W., K. A. Innanen, and Y. Geng, 2018, Elastic full-waveform inversion and parametrization analysis applied to walk-away vertical seismic profile data for unconventional (heavy oil) reservoir characterization: *Geophysical Journal International*, **213**, 1934–1968.
- Pan, W., K. A. Innanen, Y. Geng, and J. Li, 2019, Interparameter trade-off quantification for isotropic-elastic full-waveform inversion with various model parameterizations: *Geophysics*, **84**, R185–R206.
- Powell, M. J., 1969, A method for nonlinear constraints in minimization problems: *Optimization*, 283–298.
- Prioux, V., R. Brossier, Y. Gholami, S. Operto, J. Virieux, O. Barkved, and J. Kommedal, 2011, On the footprint of anisotropy on isotropic full waveform inversion: the Valhall case study: *Geophysical Journal International*, **187**, 1495–1515.
- Prioux, V., R. Brossier, S. Operto, and J. Virieux, 2013a, Multiparameter full waveform inversion of multicomponent OBC data from Valhall. Part 1: imaging compressional wavespeed, density and attenuation: *Geophysical Journal International*, **194**, 1640–1664.
- , 2013b, Multiparameter full waveform inversion of multicomponent OBC data from valhall. Part 2: imaging compressional and shear-wave velocities: *Geophysical Journal International*, **194**, 1665–1681.
- Ravaut, C., S. Operto, L. Improta, J. Virieux, A. Herrero, and P. dell’Aversana, 2004, Multi-scale imaging of complex structures from multi-fold wide-aperture seismic data by frequency-domain full-wavefield inversions: application to a thrust belt: *Geophysical Journal International*, **159**, 1032–1056.
- Sears, T., S. Singh, and P. Barton, 2008, Elastic full waveform inversion of multi-component OBC seismic data: *Geophysical Prospecting*, **56**, 843–862.
- Sun, H., and L. Demanet, 2021, Deep learning for low-frequency extrapolation of multicomponent data in elastic FWI: *IEEE Transactions on Geoscience and Remote Sensing*, **60**, 1–11.
- Sun, M., J. Yang, L. Dong, Y. Liu, and C. Huang, 2017, Density reconstruction in multiparameter elastic full-waveform inversion: *Journal of Geophysics and Engineering*, **14**, 1445–1462.
- Tarantola, A., 1984, Inversion of seismic reflection data in the acoustic approximation: *Geophysics*, **49**, 1259–1266.
- , 1986, A strategy for nonlinear inversion of seismic reflection data: *Geophysics*, **51**, 1893–1903.
- van Leeuwen, T., and F. J. Herrmann, 2013, Mitigating local minima in full-waveform inversion by expanding the search space: *Geophysical Journal International*, **195**, 661–667.
- Vigh, D., K. Jiao, D. Watts, and D. Sun, 2014, Elastic full-waveform inversion application using multicomponent measurements of seismic data collection: *Geophysics*, **79**, R63–R77.

- Virieux, J., and S. Operto, 2009, An overview of full waveform inversion in exploration geophysics: *Geophysics*, **74**, WCC1–WCC26.
- Wang, C., J. Cheng, W. W. Weibull, and B. Arntsen, 2019, Elastic wave-equation migration velocity analysis preconditioned through mode decoupling: *Geophysics*, **84**, R341–R353.
- Wang, T., and J. Cheng, 2017, Elastic full waveform inversion based on mode decomposition: The approach and mechanism: *Geophysical Journal International*, **209**, 606–622.
- Wang, T., J. Cheng, Q. Guo, and C. Wang, 2018, Elastic wave-equation-based reflection kernel analysis and travelttime inversion using wave mode decomposition: *Geophysical Journal International*, **215**, 450–470.
- Xiong, K., D. Lumley, and W. Zhou, 2023, Improved seismic envelope full waveform inversion: *Geophysics*, **88**, 1–197.
- Xu, K., and G. A. McMechan, 2014, 2D frequency-domain elastic full-waveform inversion using time-domain modeling and a multistep-length gradient approach: *Geophysics*, **79**, R41–R53.
- Zhang, W., and Y. Li, 2022, Elastic wave full-waveform inversion in the time domain by the trust region method: *Journal of Applied Geophysics*, **197**, 104540.
- Zhang, Z.-d., and T. Alkhalifah, 2019, Local-crosscorrelation elastic full-waveform inversion: *Geophysics*, **84**, R897–R908.
- Zhang, Z.-d., T. Alkhalifah, E. Z. Naeini, and B. Sun, 2018, Multiparameter elastic full waveform inversion with facies-based constraints: *Geophysical Journal International*, **213**, 2112–2127.